catalysts

MDPI

Article

Synthesis, Performance Measurement of $Dy_2EuSbO_7/ZnBiDyO_4$ Heterojunction Composite Catalyst and Photocatalytic Degradation of Chlorpyrifos within Pesticide Wastewater under Visible Light Irradiation

Jingfei Luan [1,2,*], Yang Xiao [1], Liang Hao [1], Ye Yao [1], Bowen Niu [1], Guangmin Yang [1] and Yichun Wang [1]

[1] School of Physics, Changchun Normal University, Changchun 130032, China; qx202200243@stu.ccsfu.edu.cn (Y.X.); hliang0725@163.com (L.H.); yaoye1109@mails.jlu.edu.cn (Y.Y.); niubw2021@126.com (B.N.); yangguangmin@ccsfu.edu.cn (G.Y.); yichun2000@126.com (Y.W.)
[2] State Key Laboratory of Pollution Control and Resource Reuse, School of the Environment, Nanjing University, Nanjing 210093, China
* Correspondence: jfluan@nju.edu.cn; Tel.: +86-(0)-19951939498

Abstract: For the first time, a novel catalyst named Dy_2EuSbO_7 was successfully synthesized via the high-temperature solid-state sintering method (HTSSM). $Dy_2EuSbO_7/ZnBiDyO_4$ heterojunction photocatalyst (DZHP) was fabricated through the HTSSM for degrading chlorpyrifos (CPS) in the pesticide wastewater under visible light irradiation (VSLID). Under VSLID, DZHP could effectively degrade CPS in pesticide wastewater. The experimental outcomes suggested that the kinetic curve with the $Dy_2EuSbO_7/ZnBiDyO_4$ heterojunction (DZH) as a photocatalyst for the reduction of CPS under VSLID conformed to the first-order kinetics (FOKT). After VSLID of 156 min, the photocatalytic degradation (PTD) removal rate of CPS using DZH as photocatalyst was 1.12 times, 1.21 times, or 2.96 times that using Dy_2EuSbO_7 as a photocatalyst, $ZnBiDyO_4$ as a photocatalyst, or nitrogen-doped titanium dioxide as a photocatalyst. After VSLID of 156 min for four cycle degradation tests (FCDTS) with DZH as a photocatalyst, the removal rate of CPS reached 98.78%, 97.66%, 96.59%, and 95.69%, respectively. Above results indicated that the DZHP possessed high stability. Experiments with the addition of trapping agents showed that hydroxyl radicals (•OH) owned the strongest oxidative removal ability for degrading CPS compared with superoxide anions ($\bullet O_2^-$) or holes (h^+). The oxidation capacity of three oxidation radicals for eliminating CPS was ranked in the ascending order as follows: $h^+ < \bullet OH < \bullet O_2^-$. Lastly, the possible degradation pathway and degradation mechanism of CPS were discussed in detail. A visible light responsive heterojunction catalyst with high catalytic activity and a photocatalytic reaction system which were capable of efficiently removing toxic organic pollutants from pesticide wastewater were obtained.

Keywords: Dy_2EuSbO_7; $Dy_2EuSbO_7/ZnBiDyO_4$ heterojunction photocatalyst; chlorpyrifos; photocatalytic degradation; visible light irradiation; N-doped TiO_2; degradation pathway; degradation mechanism

check for updates

Citation: Luan, J.; Xiao, Y.; Hao, L.; Yao, Y.; Niu, B.; Yang, G.; Wang, Y. Synthesis, Performance Measurement of $Dy_2EuSbO_7/ZnBiDyO_4$ Heterojunction Composite Catalyst and Photocatalytic Degradation of Chlorpyrifos within Pesticide Wastewater under Visible Light Irradiation. *Catalysts* **2024**, *14*, 646. https://doi.org/10.3390/catal14090646

Academic Editor: Pedro B. Tavares

Received: 30 July 2024
Revised: 8 September 2024
Accepted: 19 September 2024
Published: 21 September 2024

1. Introduction

Pesticides perform a significant part in the procedure of grain cultivation, and they are mainly used to control pests and disease as well as to help increase food production. However, the overuse of pesticides poses a range of problems for the environment and human health [1,2]. The residual pesticides pollute the water source and the soil [3]. Long-term exposure or consumption of food containing pesticides increases the risk of cancer and neurological diseases [4–6]. Pesticides thereby endanger the biodiversity of the natural world.

Chlorpyrifos (CPS) is a widely used insecticide with a strong poisoning effect on insects and a long validity period; moreover, CPS is difficult to be degraded [7–9]. CPS affects the activity of soil microorganisms and changed the functions of the soil; thus, plant growth is affected. In addition, CPS could enter the human body through water sources or the food chain; thus, CPS could cause a potential threat to human health [10,11]. Therefore, the degradation of CPS is necessary.

Various methods are currently available to degrade CPS, which are derived from the pesticide wastewater, such as physical methods, chemical methods, and biological methods [12,13]. Physical methods include the adsorption method, ion exchange method, and membrane method. Chemical methods include the chemical precipitation method, electrochemical method, and chemical redox method. Biological methods are mainly divided into anaerobic methods and aerobic methods. Physical methods could achieve better results, but these technologies cannot completely eliminate CPS, and the material consumption of physical methods is large, which increases the treatment cost. The chemical redox method possesses a high cost and low efficiency; simultaneously, the chemical redox method also causes secondary pollution problems. Biological methods have long treatment cycles and are difficult to utilize for treating toxic and non-biodegradable organic contaminants. Obviously, the above-mentioned methods possess many disadvantages.

Some advanced oxidation techniques, such as the photocatalytic oxidation method, Feton, and supercritical water oxidation, possess incomparable advantages for the degradation of CPS due to their powerful oxidation capacity and extremely high reaction accuracy [14–23]. Photocatalytic technology utilizes sunlight as energy to activate photocatalysts; as a result, oxidized groups could be produced under the irradiation of light, and CPS could be effectively removed; meanwhile, the photocatalysts could be recycled. Therefore, the photocatalytic oxidation method is widely used in wastewater treatment [24]. The significant challenge for the industrialization application of photocatalytic technology is to develop optimal photocatalysts, which should possess four essential characteristics as follows: a high photocatalytic efficiency, a substantial specific surface area, comprehensive utilization of sunlight, and recyclability [25–28]. In addition, the photocatalytic activity is intricately associated with the dimensions, shape, bandgap, and crystalline configuration of the photocatalyst. The development of TiO_2, which belongs to the most commonly used metal oxide photocatalyst, is limited because TiO_2 is only able to absorb UV light, which makes up 5% of solar energy [29–37]; consequently, TiO_2 cannot effectively harness light energy. Therefore, developing visible light responsive photocatalysts and improving the photonic efficiency of photocatalysts are inevitable trends in the field of photocatalysis research.

As per earlier reports, it is generally believed that the metal oxide compounds ABO_3, ABO_4 and $A_2B_2O_7$ [38–43] have photocatalytic performance under visible light irradiation (VSLID). Tong et al. conducted photocatalytic experiments on $BiFeO_3$ wafers under VSLID and achieved good results [38]. Hu et al. investigated how the $BiVO_4$ catalyst affected the rate at which acetaminophen degraded under VSLID. [40]. Zhang et al. synthesized porous $Sm_2Ti_2O_7$ material using the sol-gel technique with PEG4000 as the template; consequently, the $Sm_2Ti_2O_7$ with a thermal feldspar structure promoted the crystallization of porous samples; thereby, the catalytic efficiency was improved [42]. In an effort to produce a photocatalyst with excellent performance and visible light response, Luan et al. prepared a Fe_2BiSbO_7 photocatalyst and explored its characteristics and photocatalytic activity; as a result, good results were achieved [43]. In our previous work [44], we found that Bi_2GaSbO_7 crystals possessed a thermal feldspar shape structure and could serve as efficient photocatalysts under VSLID. After changing the structure of Bi_2GaSbO_7, the novel photocatalyst had the capacity to increase the activity of the photocatalysts. Considering the analysis above, we can conclude that replacing Fe^{3+} with Bi^{3+} and replacing Bi^{3+} with Ga^{3+} in Fe_2BiSbO_7, as well as the synthetical Bi_2GaSbO_7, might enhance the carrier concentration. In a similar way, by replacing Bi^{3+} with Dy^{3+} and replacing Ga^{3+} with Eu^{3+} in Bi_2GaSbO_7, the synthetical Dy_2EuSbO_7 might also ultimately enhance the carrier concentration. Therefore, the novel Dy_2EuSbO_7 compound's electrical transport and photophysical characteristics would undergo changes and improvements; as a result, advanced photocatalytic performance could be achieved.

Many methods have been proven effective for improving photonic efficiency, such as ion doping, heterojunction construction, and photosensitization [45–53]. Among the various available methods, the construction of heterojunctions remains an actively promising research area within the domain of photocatalysis [54–59]. Heterojunction catalysts combine what comes out of one photocatalyst and results in higher light utilization efficiency, higher photocatalytic performance, and higher chemical stability of the composite system, as well as a longer service life. Xu et al. prepared n-n type heterojunction $ZnFe_2O_4/BiVO_4$ using chemical co-precipitation method; as a result, the experiments showed that the heterojunctions exhibited higher photocatalytic activity compared with pure $BiVO_4$ or $ZnFe_2O_4$ because heterojunctions could generate more photoinduced electrons (e^-) [60]. Ma synthesized a p-n heterojunction NiO_x/Bi_2WO_6, and the enhanced photocatalytic performance of NiO_x/Bi_2WO_6 samples was attributed to the p-n junction between Bi_2WO_6 and NiO_x, which enhanced the photoinduced e^- and photoinduced hole (h^+) separation efficiency [61]. By analyzing above results, we can conclude that constructing heterojunctions increased the photocatalysts' redox performance [62–66]; ultimately, the reaction's overall selectivity and activity were enhanced. Therefore, the $Dy_2EuSbO_7/ZnBiDyO_4$ heterojunction photocatalyst (DZHP) can also be synthesized, and the photocatalytic performance for CPS degradation is worth exploring.

This paper analyzed the structural characteristics of pure-phase $ZnBiDyO_4$ and single-phase Dy_2EuSbO_7 which were prepared by the high-temperature solid-state sintering method (HTSSM) through an X-ray diffractometer (XRD), UV-Vis spectrophotometer, Fourier transform infrared (FTIR) spectrometer, Raman spectrometer, X-ray photoelectron spectroscopy (XPS), transmission electron microscopy (TEM), and energy dispersive X-ray spectroscopy (EDS). In addition, the removal efficiency of CPS under VSLID was investigated using Dy_2EuSbO_7 or $ZnBiDyO_4$ or N-doped TiO_2 or $Dy_2EuSbO_7/ZnBiDyO_4$ heterojunction (DZH) as a photocatalyst. The purpose of this study was to prepare a novel heterojunction catalyst for the removal of CPS from pesticide wastewater under VSLID. The innovation idea of this study lies in the first synthesis of the new Dy_2EuSbO_7 nanocatalyst and DZHP using HTSSM. DZHP is a visible-light-responsive photocatalyst with high photocatalytic activity and can effectively remove CPS from pesticide wastewater. This study makes the removal of organic pollutants from pesticide wastewater more efficient and safer.

2. Results and Discussion

2.1. XRD Analysis

Figure 1 shows the XRD patterns of DZHP, Dy_2EuSbO_7, $ZnBiDyO_4$, and N-doped TiO_2. Data were analyzed using Materials Studio. Figure 2a shows the crystallization of Dy_2EuSbO_7, with an R_p factor of 5.20%. Figure 2b illustrates the atomic structure of Dy_2EuSbO_7. It could be found from Figure 2 that Dy_2EuSbO_7 possessed the perfect degree of crystallinity, meanwhile, Dy_2EuSbO_7 owned a pyrrhotite-type structure with a spatial group of *Fd3m*, belonged to a cubic crystal system, and possessed a lattice parameter of 10.4440423 Å. Figure 3a shows the crystallization of $ZnBiDyO_4$, with an R_p factor of 7.20%. Figure 3b illustrates the atomic structure of $ZnBiDyO_4$. It could be found from Figure 3 that $ZnBiDyO_4$ was a single-phase high-purity compound and owned perfect degree of crystallinity; simultaneously, $ZnBiDyO_4$ possessed a spinel structure with a spatial group of *I41/Amd*, belonged to a tetragonal system, and owned a lattice parameter of a = b = 10.541001 Å and c = 9.930823 Å. According to Figures 2 and 3, the indices of crystallographic plane value for the principal diffraction peaks of Dy_2EuSbO_7 or $ZnBiDyO_4$ were calculated and labelled. Table 1 presents comprehensive details on the atomic coordinates and structural parameters of Dy_2EuSbO_7. Table 2 presents comprehensive details on the atomic coordinates and structural parameters of $ZnBiDyO_4$. Furthermore, as shown in Figure 1d, the peak of the nitrogen-doped TiO_2 sample prepared corresponds to the anatase TiO_2 phase. We have also successfully synthesized N-doped TiO_2.

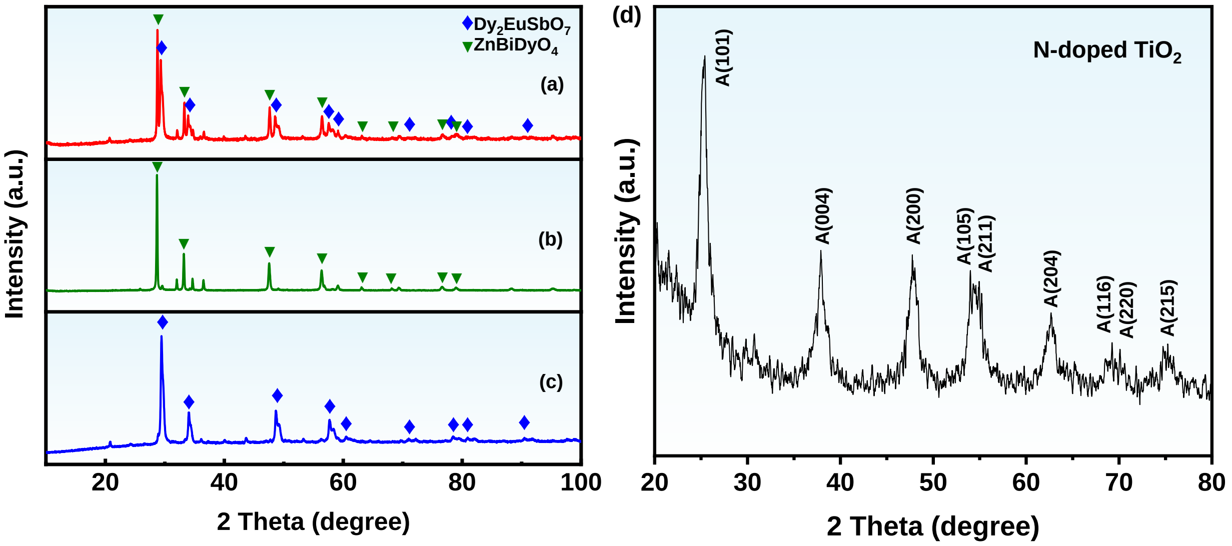

Figure 1. XRD patterns: (**a**) DZHP, (**b**) $ZnBiDyO_4$, (**c**) Dy_2EuSbO_7, (**d**) N-doped TiO_2.

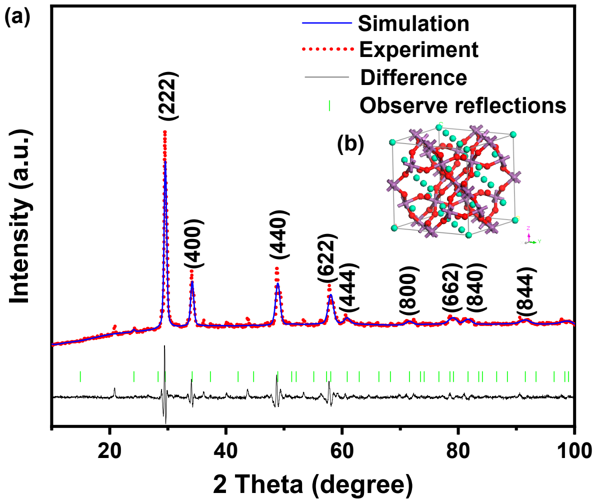

Figure 2. (**a**) XRD patterns and Rietveld refinement and (**b**) the atomic structure (red atom: O, purple atom: Eu or Sb, green atom: Dy) of Dy_2EuSbO_7.

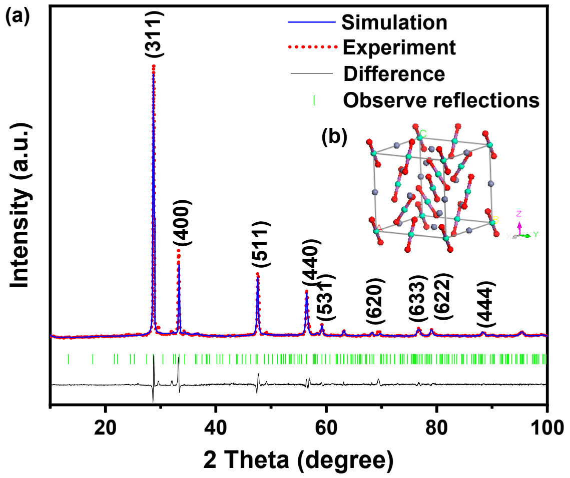

Figure 3. (**a**) XRD patterns and Rietveld refinement and (**b**) the atomic structure (red atom: O, green atom: Zn, purple atom: Bi or Dy) of $ZnBiDyO_4$.

Table 1. Structural parameters of Dy_2EuSbO_7 prepared by the solid-phase sintering method.

Atom	x	y	z	Occupation Factor
Dy	0	0	0	1
Eu	0.5	0.5	0.5	0.5
Sb	0.5	0.5	0.5	0.5
O(1)	−0.185	0.125	0.125	1
O(2)	0.125	0.125	0.125	1

Table 2. Structural parameters of $ZnBiDyO_4$ prepared by the solid-phase sintering method.

Atom	x	y	z	Occupation Factor
Zn	0	0	0.5	1
Bi	0	0	0	1
Dy	0	0	0	1
O	0.76731	0.14013	0.08188	1

Insights into the octahedral deformation of MO_6 (M = Eu^{3+} and Sb^{5+}) could be derived from the x-coordinate value [58]. The x-value shifted from x = 0.375 [67], so the distortion of the MO_6 (M = Eu^{3+} and Sb^{5+}) octahedral was clearly present in the crystal structure of Dy_2EuSbO_7. In order to prevent photogenerated h^+ from recombining with photogenerated e^-, achieving charge separation became imperative for the photocatalytic decomposition of CPS under VSLID. According to Inoue and Kudo, the key to reducing charge recombination and boosting photocatalytic effectiveness is the local distortion of MO_6 octahedra derived from photocatalysts such as $BaTi_4O_9$ and $Sr_2M_2O_7$ (M = Nb^{5+} and Ta^{5+}). [68,69]. Therefore, the distortion of MO_6 (M = Eu^{3+} and Sb^{5+}) octahedrals in the crystal structure of Dy_2EuSbO_7 could also be used to enhance photocatalytic activity. Dy_2EuSbO_7 consisted of a three-dimensional mesh structure of MO_6 (M = Eu^{3+} and Sb^{5+}) octahedrals that shared angles. MO_6 (M = Eu^{3+} and Sb^{5+}) octahedrals were linked into chains by Eu^{3+} ions. Two Dy-O bond lengths coexisted: six Dy-O(1) bond lengths (2.769 Å) were significantly longer than two Dy-O(2) bond lengths (2.472 Å). Six M-O(1) (M = Eu^{3+} and Sb^{5+}) bond lengths were 2.569 Å long, and M-Dy (M = Eu^{3+} and Sb^{5+}) bond lengths were 3.647 Å long. The M-O-M (M = Eu^{3+} and Sb^{5+}) bond angle in the Dy_2EuSbO_7 crystal structure was 139.211°. The Dy-M-Dy (M = Eu^{3+} and Sb^{5+}) bond angle was 135.425° in the Dy_2EuSbO_7 crystal structure. The Dy-M-O (M = Eu^{3+} and Sb^{5+}) bond angle was 133.688° in the Dy_2EuSbO_7 crystal structure. Research on luminescence characteristics found that more excited states were delocalized the closer the M-O-M bond angle was to 180° [70]. The results showed that the angle between MO_6 (M = Eu^{3+} and Sb^{5+}) octahedrals with shared angles, such as the M-O-M bond angle of Dy_2EuSbO_7, was of great significance for affecting the photocatalytic activity of Dy_2EuSbO_7.

2.2. FTIR Analysis

In an effort to determine which chemical bonds and functional groups exist in DZHP, an FTIR spectrometer was used to produce the FTIR spectra of Dy_2EuSbO_7 and $ZnBiDyO_4$, as seen in Figure 4. DZHP, Dy_2EuSbO_7, and $ZnBiDyO_4$ all displayed many distinctive absorption peaks in their FTIR spectra. These included peaks related to Dy-O, Eu-O, Sb-O, Sb-O-Sb, Zn-O, and Bi-O bonds. The stretching vibration of Dy-O was observed at 613 cm^{-1} [43,60], while the bending vibration of Eu-O occurred at 590 cm^{-1} [71]. The stretching vibration of Zn-O occurred at 468 cm^{-1} [72], while the bending vibration of Bi-O was associated with peaks at 428 cm^{-1} [73,74], and the bending vibration of Sb-O was observed at 458 cm^{-1} and 583 cm^{-1} [75]. The bending vibration of Sb-O-Sb was represented by peaks at 658 cm^{-1} [76]. Furthermore, the broad peak observed at 3431 to 3576 cm^{-1} indicated the stretching vibrations of O-H groups from chemisorbed water molecules [77,78]. The peak at 1632 cm^{-1} corresponded to the bending vibration mode of these O-H groups [79]. The multiple bands observed at 1379 to 1632 cm^{-1} were attributed to the vibrations of C-H bonds from adsorbed water [80,81].

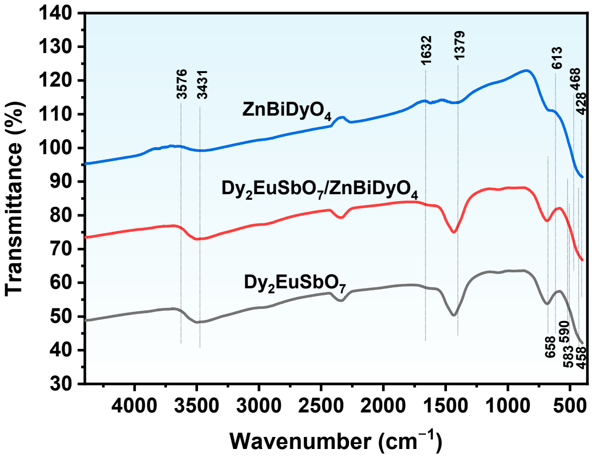

Figure 4. FTIR spectra of Dy_2EuSbO_7, $ZnBiDyO_4$, and DZHP.

2.3. Raman Analysis

Raman spectra were obtained using a Raman spectrometer to analyze the interactions between various chemical bonds in DZHP, Dy_2EuSbO_7, and $ZnBiDyO_4$. The Raman spectra of $ZnBiDyO_4$, Dy_2EuSbO_7, and DZHP are shown in Figure 5. The Raman spectrum of Dy_2EuSbO_7 exhibited characteristic modes, including the E_{1g} main vibrational modes at 542 cm^{-1}, associated with the stretching vibration of Eu-O bonds, as well as the peaks at 199cm^{-1} [82], associated with the stretching vibration of Dy-O bonds [83]. Additionally, peaks at 368 cm^{-1}, 654 cm^{-1}, and 719 cm^{-1} could be assigned to the bend vibration of Sb-O and Sb-O-Sb [84,85]. The Raman spectra of $ZnBiDyO_4$ revealed a broad band at 128 cm^{-1}, 637 cm^{-1}, and 843 cm^{-1}, which could be attributed to the stretching vibrations of Dy-O, Bi-O, and Zn-O, respectively [83–88]. Notably, the Raman spectra of DZHP exhibited strong peaks encompassing the distinct absorption peaks of both Dy_2EuSbO_7 and $ZnBiDyO_4$, including peaks at 136 cm^{-1}, 192 cm^{-1}, 370 cm^{-1}, 533 cm^{-1}, 640 cm^{-1}, 713 cm^{-1}, and 839 cm^{-1}.

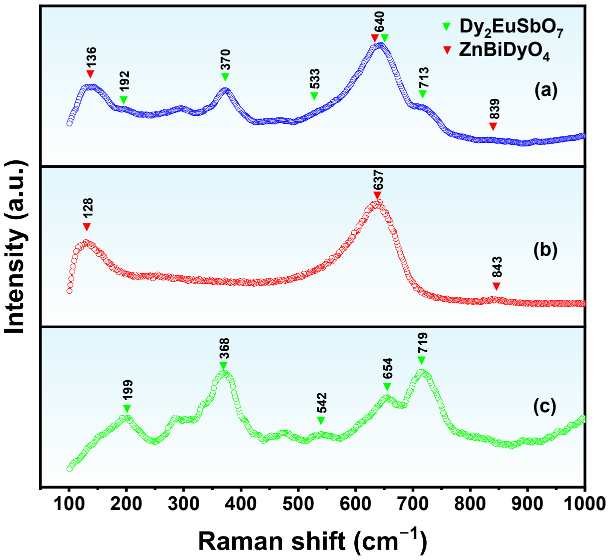

Figure 5. Raman spectra of (**a**) DZHP, (**b**) Dy_2EuSbO_7, and (**c**) $ZnBiDyO_4$.

2.4. UV-Vis Diffuse Reflectance Spectra

The absorption spectra of DZHP, Dy_2EuSbO_7, and $ZnBiDyO_4$ sample are shown in Figure 6a. The absorption edges of DZHP, Dy_2EuSbO_7, and $ZnBiDyO_4$ were located at 595 nm, 430 nm, and 590 nm, which were all in the visible region of the spectrum. The band gap energies of the crystalline semiconductors could be determined by the intersection point between photon energy hν axis and the line extrapolated from the linear portion of the absorption edge of the so-called Kubelka–Munk function (1) (known as the re-emission function) [89]:

$$\frac{[1 - R_d(h\nu)]^2}{2R_d(h\nu)} = \frac{\alpha(h\nu)}{S} \tag{1}$$

where S was the scattering factor, and R_d was the diffuse reflectance, and α represented absorption coefficient of radiation.

The optical absorption near the band edge of the crystalline semiconductors obeyed Equation (2) [90,91]:

$$\alpha h\nu = A\,(h\nu - E_g)^n \tag{2}$$

Here, A, α, E_g, and ν denote the proportional constant, absorption coefficient, band gap, and light frequency, respectively. Within this equation, n determined the character of the transition in a semiconductor. The E_g values of Dy_2EuSbO_7 and $ZnBiDyO_4$ were 2.68 eV and 1.78 eV, respectively. The E_g value of DZHP was 1.75 eV. As shown in Figure 6b, the estimated (n) value was roughly 0.5, which proves that the phototransition mode of the catalyst was a direct transition. Moreover, the absorption spectrum of N-doped TiO_2 is shown in Figure 6c. The absorption edge of N-doped TiO_2 was located at 421 nm, also in the visible region of the spectrum.

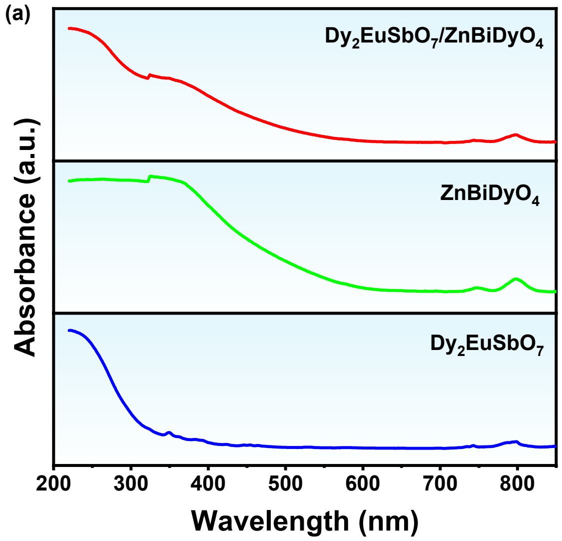

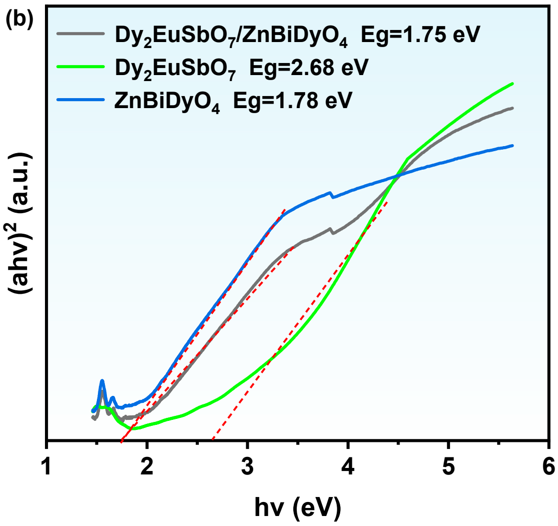

Figure 6. *Cont.*

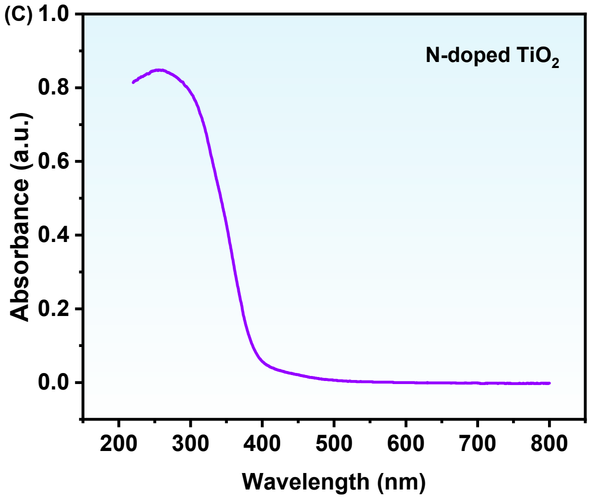

Figure 6. (**a**) The UV-Vis diffuse reflectance spectra of the synthesized DZHP, Dy_2EuSbO_7, and $ZnBiDyO_4$; (**b**) correlative diagram of $(\alpha h\nu)^2$ and hν of the synthesized DZHP, Dy_2EuSbO_7, and $ZnBiDyO_4$; and (**c**) the UV-Vis diffuse reflectance spectra of N-doped TiO_2.

2.5. Property Characterization of Dy_2EuSbO_7/$ZnBiDyO_4$ Heterojunction Photocatalyst

To determine the surface chemical composition and valence states of DZHP, Dy_2EuSbO_7 and $ZnBiDyO_4$, X-ray photoelectron spectroscopy (XPS) was used. Figure 7 displays the XPS spectra of DZHP, Dy_2EuSbO_7, and $ZnBiDyO_4$. It was evident that Dy, Eu, Sb, Zn, Bi, and O elements were present in DZHP, indicating that heterojunction structures had been successfully constructed. As a reference for calibration, there was an observable carbon peak.

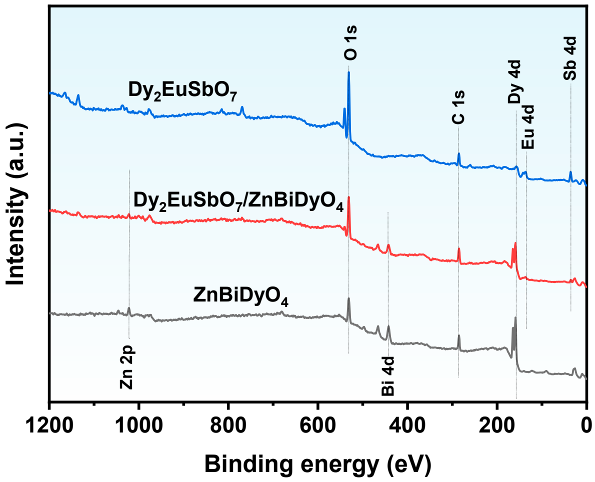

Figure 7. The XPS full spectrum of the synthesized DZHP, Dy_2EuSbO_7, and $ZnBiDyO_4$.

Figure 8a–f show the XPS spectra of Dy_2EuSbO_7 and $ZnBiDyO_4$ component elements. Based on the XPS analysis results, the peaks of various elements with specific binding energy were obtained, among which the Dy $4d_{5/2}$ peak of Dy element was located at 159.09 eV, and the Eu $4d_{5/2}$ peak of Eu element was located at 136.02 eV. The Sb $4d_{3/2}$ peak of the Sb element was 34.96 eV. The Zn $2p_{3/2}$ peak of Zn was 1022.13 eV. The Bi $4d_{5/2}$ peaks of Bi elements were located at 442.21 eV. A slight shift of these peaks toward higher binding energy was observed when compared with the XPS spectrum of DZHP. These shifts indicate the presence of strong interfacial interactions between Dy_2EuSbO_7 and $ZnBiDyO_4$, which might be have been due to e^- transfer and delocalization between the two components in the heterojunction photocatalytic materials [92].

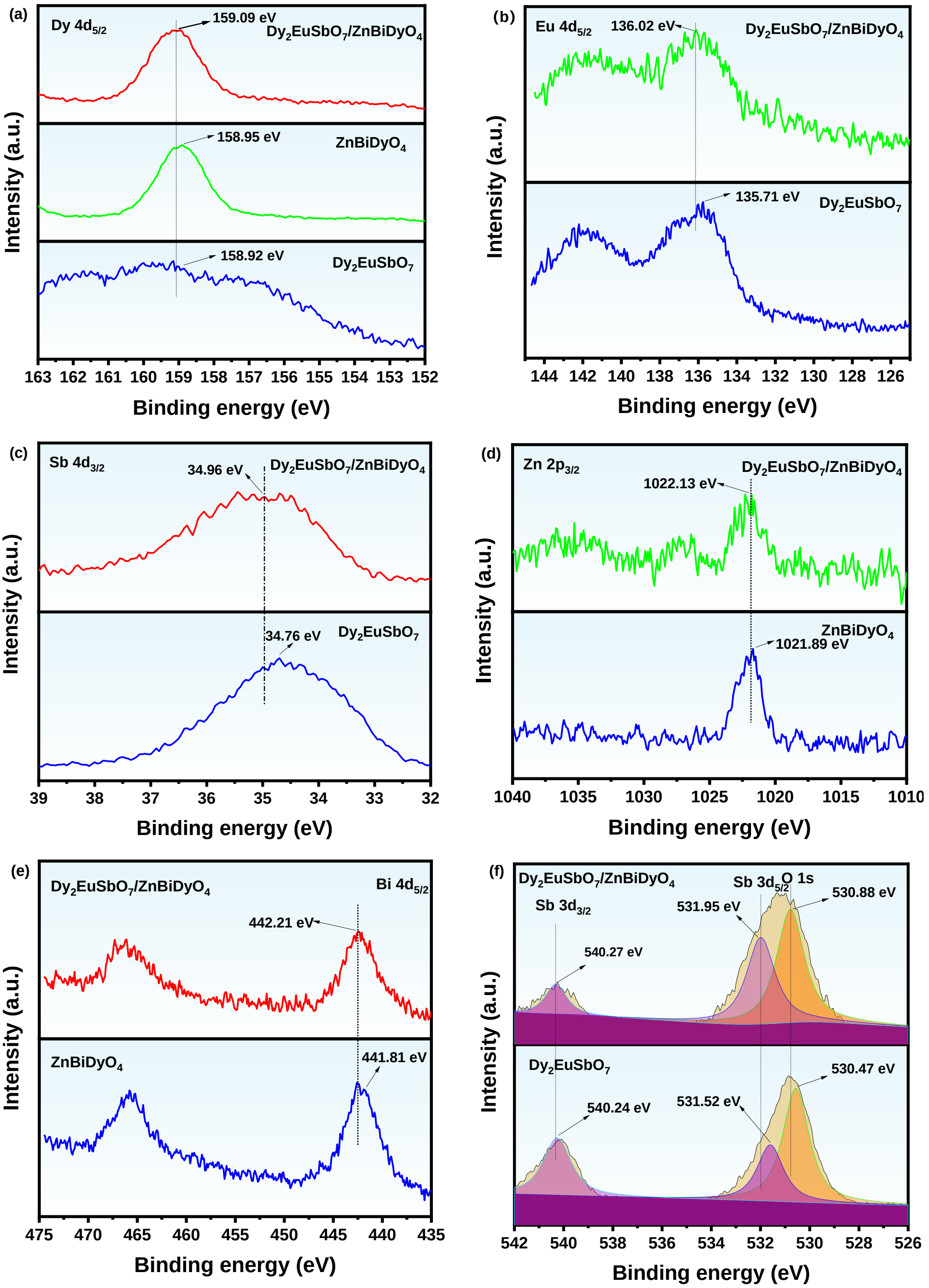

Figure 8. The corresponding high-resolution XPS spectra of (**a**) Dy 4d, (**b**) Eu 4d, (**c**) Sb 4d, (**d**) Zn 2p, (**e**) Bi 4d, (**f**) O 1s of DZHP, Dy_2EuSbO_7, and $ZnBiDyO_4$.

Figure 8f shows the O 1s spectra of DZHP and Dy_2EuSbO_7. They were located at 530.88 eV and 530.47 eV, respectively. The Sb $3d_{5/2}$ peaks of Sb elements were located at 531.95 eV and 531.52 eV. The Sb $3d_{3/2}$ peaks of Sb were located at 540.27 eV and 539.24 eV. Similarly, the spin-orbit separation value between Sb $3d_{5/2}$ and Sb $3d_{3/2}$ was observed to be 8.36 eV for Dy_2EuSbO_7 and DZHP, confirming the exclusive presence of Sb^{5+} [93,94].

From the XPS analysis findings, it is evident that the oxidation states of Dy, Eu, Zn, Bi, Sb, and O ions were +3, +3, +2, +3, +5, and −2, respectively. The surface elemental analysis results showed that the average atomic ratio of Dy:Eu:Sb:Zn:Bi:O was 1920:1010:890:650:390:5150. The atomic ratios of Dy:Eu:Sb and Zn:Bi:Dy in the samples of DZHP were 1.95:0.96:1.00 and 1.00:0.96:0.98, respectively. The high oxygen content was due to the large amount of oxygen adsorbed on the surface of DZHP. Apparently, no heteropeaks were observed in the XPS peak of the DZHP, suggesting that there were no other elements.

Figure 9a,b show the TEM images of DZHP, while Figure 9c,d show the TEM images of Dy_2EuSbO_7 and the electron diffraction patterns of the selected regions. Figure 9e,f show the TEM image of $ZnBiDyO_4$ and the electron diffraction pattern of the selected region. Figure 10 shows the EDS elemental mapping of DZHP (Dy, Eu, Sb, O from Dy_2EuSbO_7 and Zn, Bi, Dy, O from $ZnBiDyO_4$). Figure 11 presents the EDS spectra of DZHP. Based on Figures 9 and 10, the larger tetragonal particles were identified as Dy_2EuSbO_7, and the smaller circular-shaped particles were identified as $ZnBiDyO_4$. Figures 9 and 10 show Dy_2EuSbO_7 particles with a rhombic dodecahedral shape surrounded by smaller $ZnBiDyO_4$ particles. This close encapsulation indicates the successful synthesis of DZHP. It is widely recognized that the structural growth of photocatalysts is regulated by the different surface energies of microcrystalline faces [87,88], resulting in the rhombic dodecahedral morphology of Dy_2EuSbO_7. The experimental results shown in Figure 9 indicate that $ZnBiDyO_4$ exhibited a regular spherical morphology and uniform particle distribution. The particle size of $ZnBiDyO_4$ was approximately 420 nm, whereas the particle size of Dy_2EuSbO_7 was about 798 nm. The lattice parameters of Dy_2EuSbO_7 have been proven to be a = b = c = 1.0444 nm. The lattice parameters of $ZnBiDyO_4$ have been proven to be a = b = 1.0541 nm, c = 0.99308 nm. According to the calculation results in Figure 9, the same diffraction peaks as the main diffraction peaks of Dy_2EuSbO_7 in Figure 2 and $ZnBiDyO_4$ in Figure 3 could be found. Additionally, high-resolution TEM (HRTEM) images in Figure 9b reveal that the interplanar spacings (d-values) for Dy_2EuSbO_7 and $ZnBiDyO_4$ were 0.303 nm and 0.196 nm, respectively, and that the two interfaces were in close contact. This further confirms the successful synthesis of DZHP.

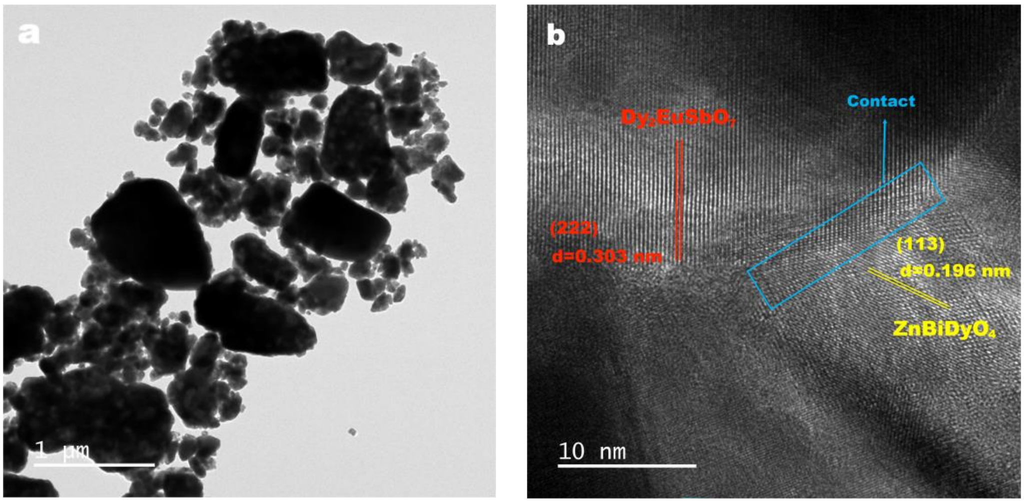

Figure 9. *Cont.*

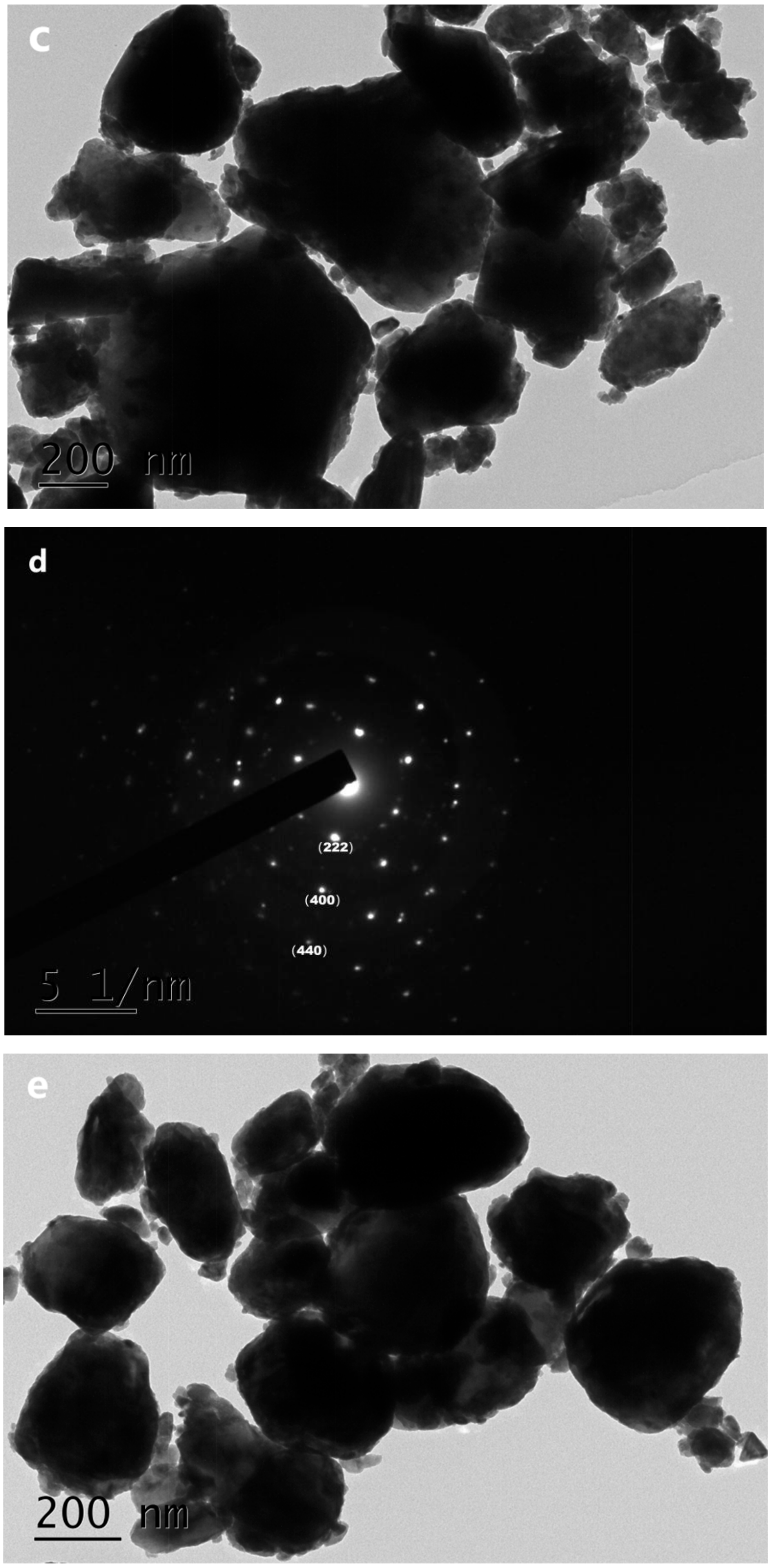

Figure 9. *Cont.*

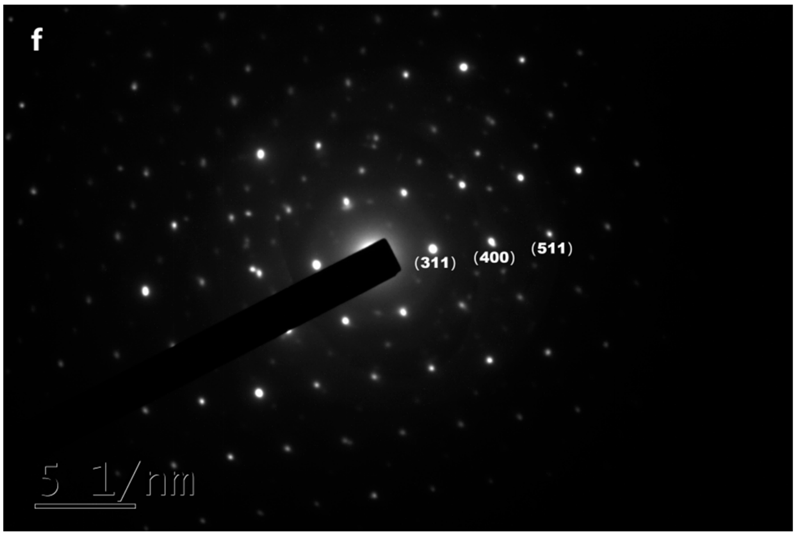

Figure 9. (**a**) TEM photograph of DZHP, (**b**) HRTEM photograph of DZHP, (**c**) TEM photograph of Dy_2EuSbO_7, (**d**) a selected area's electron diffraction pattern of Dy_2EuSbO_7, (**e**) TEM photograph of $ZnBiDyO_4$, and (**f**) a selected area's electron diffraction pattern of $ZnBiDyO_4$.

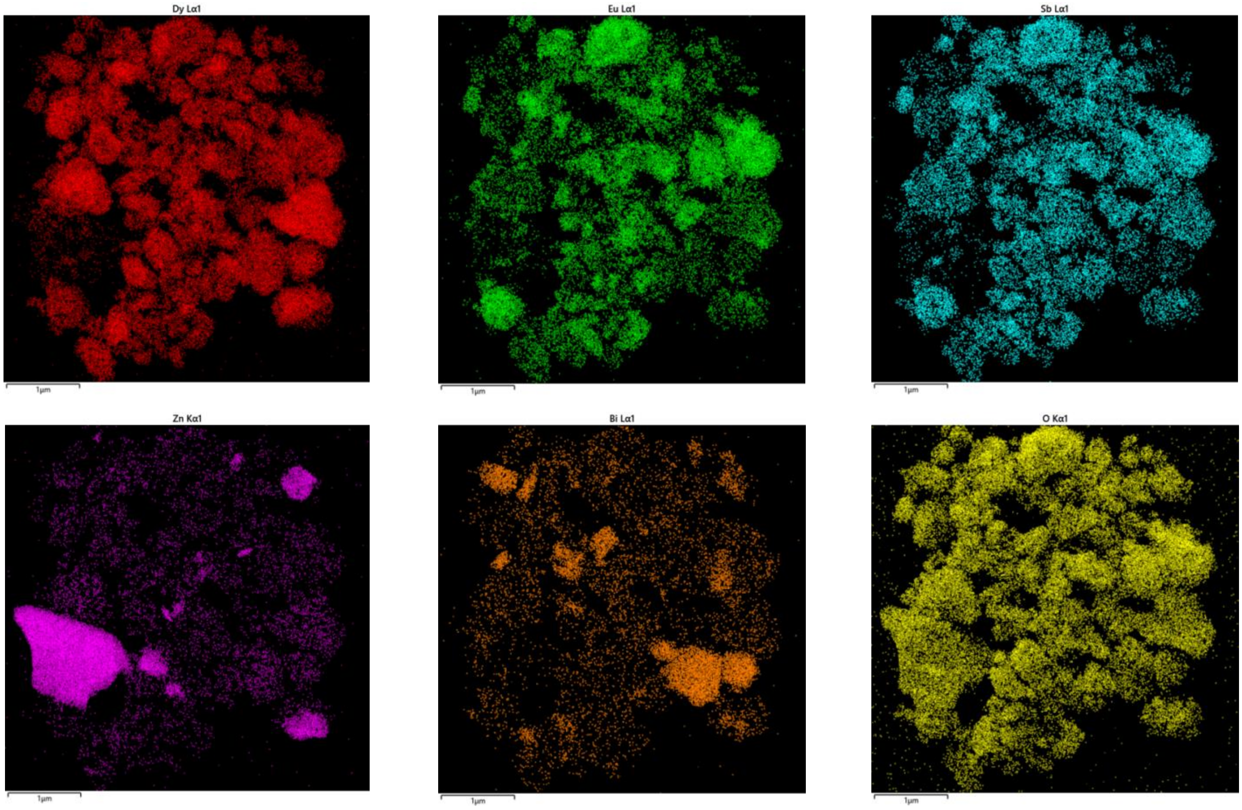

Figure 10. EDS elemental mapping of DZHP (Dy, Eu, Sb, O from Dy_2EuSbO_7 and Zn, Bi, Dy, O from $ZnBiDyO_4$).

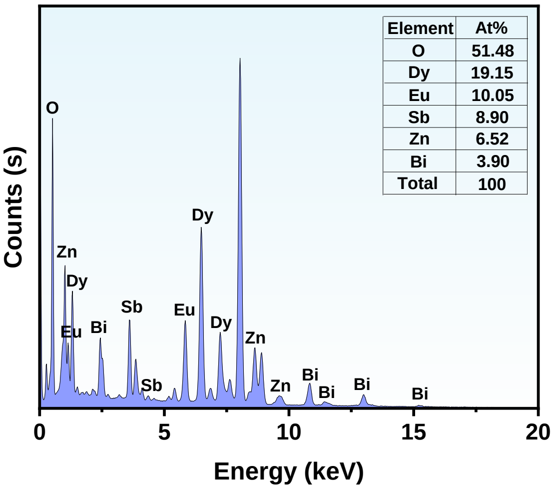

Figure 11. EDS spectrum of DZHP.

The TEM-EDS analysis showed that no other impurity elements were detected in DZHP compound. In addition, the measured pure phase of Dy_2EuSbO_7 aligned with the X-ray diffraction analysis results presented in Figure 1. By observing Figures 10 and 11, it could be clearly identified that the DZHP contained dysprosium, europium, antimony, zinc, bismuth, and oxygen. These findings were consistent with the XPS results of DZHP, as shown in Figures 7 and 8. Further analysis of the EDS spectra of DZHP showed that the atomic ratio of Dy:Eu:Sb:Zn:Bi:O was 1920:1010:890:650:390:5150, which agreed with the DZHP XPS findings. In addition, we also found that the atomic ratio of Dy_2EuSbO_7:$ZnBiDyO_4$ was close to 1.9:1. The findings of the study above allow us to infer that under the current preparation conditions, DZHP had high purity.

2.6. Photocatalytic Activity

Figure 12a shows the concentration change curves of CPS after photocatalytic degradation (PTD) of CPS under VSLID conditions using DZH, Dy_2EuSbO_7, $ZnBiDyO_4$, or N-doped TiO_2 as the photocatalyst. From Figure 12a, it is evident that the concentration of CPS within pesticide wastewater gradually decreased with increasing VSLID time. The findings derived from Figure 12a demonstrate that 99.81% of the CPS in pesticide wastewater was removed, the rate of reaction was 3.41×10^{-9} $mol{\cdot}L^{-1}{\cdot}s^{-1}$, and the photonic efficiency was 0.0716% with DZHP as the catalyst after VSLID of 156 min. And all the other experiments followed the same VSLID time of 156 min. When Dy_2EuSbO_7 was used as photocatalyst, the removal rate of CPS reached 89.09%, the rate of reaction was 3.05×10^{-9} $mol{\cdot}L^{-1}{\cdot}s^{-1}$, and the photonic efficiency was 0.0641%. The removal rate of CPS within pesticide wastewater reached 82.16%, the rate of reaction was 2.81×10^{-9} $mol{\cdot}L^{-1}{\cdot}s^{-1}$, and the photonic efficiency was 0.0590% with $ZnBiDyO_4$ as the photocatalyst. The removal rate of CPS reached 33.69%, the rate of reaction was 1.15×10^{-9} $mol{\cdot}L^{-1}{\cdot}s^{-1}$, and the photonic efficiency was 0.0242% with N-doped TiO_2 as the photocatalyst. The aforementioned findings demonstrate that, after a 156 min VSLID, the removal rate of CPS using DZHP was 1.12 times, 1.21 times, or 2.96 times greater than that using Dy_2EuSbO_7, $ZnBiDyO_4$, or N-doped TiO_2 as photocatalysts. Figure 12b shows the concentration change curve of CPS after nonilluminated adsorption by DZH, Dy_2EuSbO_7, $ZnBiDyO_4$, or N-doped TiO_2 under dark conditions. Table 3 shows the specific surface area (SSA), total pore volume (V), and average pore size (D) of the samples determined by nitrogen adsorption. After 45 min of no light adsorption, the adsorption rates of DZH, Dy_2EuSbO_7, $ZnBiDyO_4$, and N-doped TiO_2 for CPS were 4.81%, 5.28%, 5.47%, and 8.28%, respectively. It could be seen that N-doped TiO_2 had the highest dark adsorption rate, which could be attributed to its higher specific surface area.

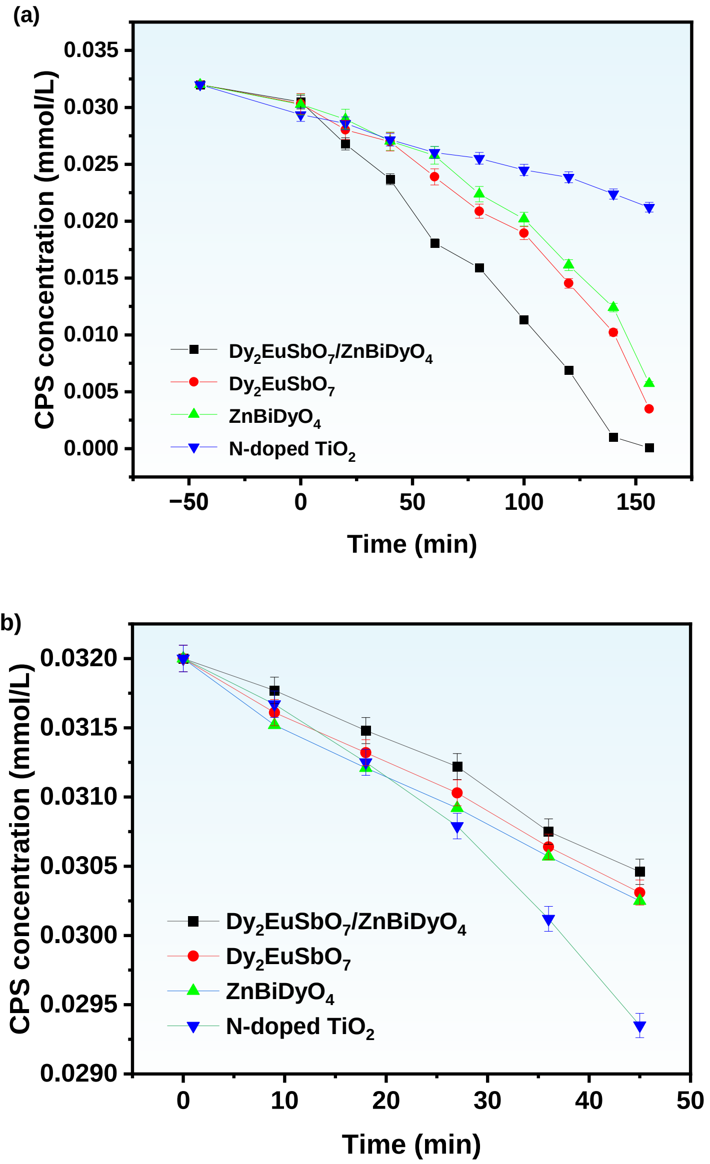

Figure 12. (**a**) Concentration variation curves of CPS during PTD with DZHP or with Dy_2EuSbO_7 as the photocatalyst or with $ZnBiDyO_4$ as the photocatalyst or with N-doped TiO_2 as the photocatalyst under VSLID. (**b**) Concentration change curve of CPS after nonilluminated adsorption by DZH, Dy_2EuSbO_7, $ZnBiDyO_4$, or N-doped TiO_2 under dark conditions.

Table 3. Specific surface area (SSA), total pore volume (V), and average pore size (D) of the samples, determined by nitrogen adsorption.

Samples	SSA (m^2/g)	V (mL/g)	D (nm)
DZHP	1.7311	0.0124	28.6523
Dy_2EuSbO_7	1.9762	0.0123	24.8963
$ZnBiDyO_4$	2.6984	0.0288	42.6920
N-doped TiO_2	45.1082	0.0212	6.9609

Figure 13 shows the change of total organic carbon (TOC) concentration when CPS in pesticide wastewater was degraded by different photocatalysts under VSLID conditions. As VSLID time increased, the concentration of CPS decreased gradually. After 156 min of VSLID, for DZHP, the TOC removal rates of Dy_2EuSbO_7, $ZnBiDyO_4$ and N-doped TiO_2 were

97.32%, 84.56%, 77.63% and 28.57%, respectively. DZHP had the highest mineralization rate during CPS degradation.

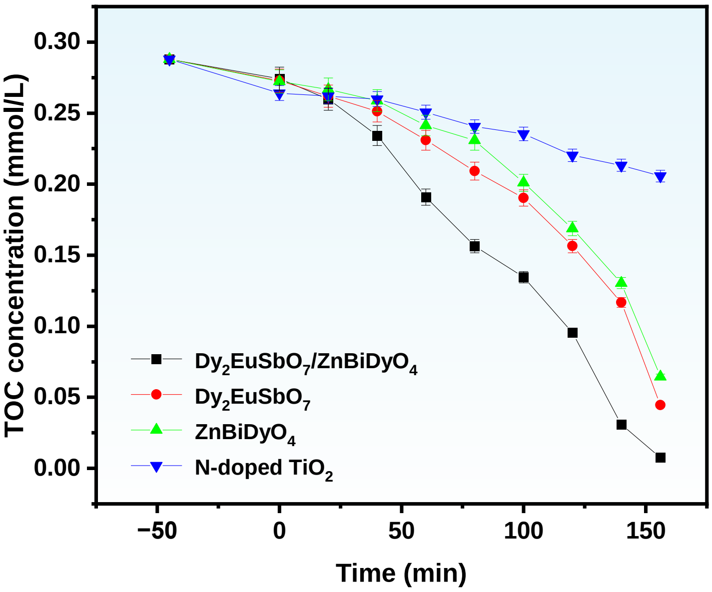

Figure 13. Concentration variation curves of TOC during PTD of CPS in pesticide wastewater with DZH, Dy_2EuSbO_7, $ZnBiDyO_4$, or N-doped TiO_2 as the photocatalyst under VSLID.

Figure 14 shows the concentration curve of CPS under VSLID during PTD of DZHP, and four-cycle degradation tests (FCDTS) were performed. The removal rate of CPS reached 98.78% or 97.66% or 96.59% or 95.69% after irradiation with DZHP for 156 min after irradiation with DZHP after completing FCDTS of CPS. Figure 15 shows the concentration curve of TOC during PTD of CPS and DZHP under VSLID, and FCDTS were performed. As illustrated in Figure 15, the removal rates of TOC were 96.25%, 95.18%, 94.16%, and 93.25%, respectively. The experimental results from Figures 15 and 16 indicate that DZHP exhibited high stability.

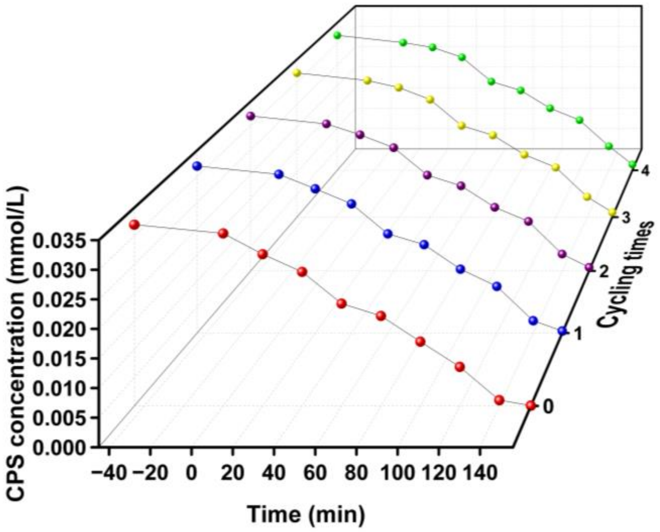

Figure 14. Concentration variation curves of CPS during PTD of CPS in pesticide wastewater with DZH as the photocatalyst under VSLID for FCDTS.

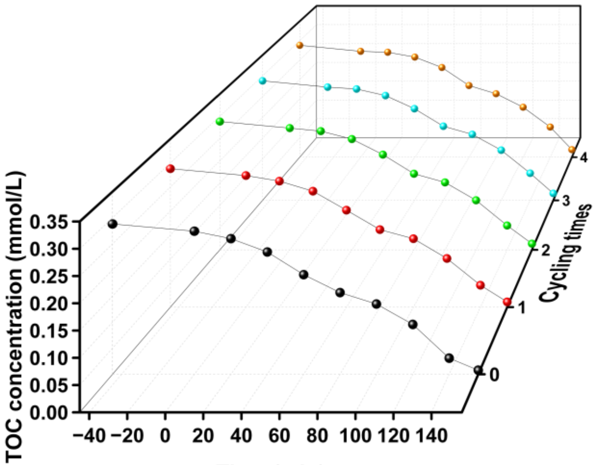

Figure 15. Concentration variation curves of TOC during PTD of CPS in pesticide wastewater with DZH as the photocatalyst under VSLID for FCDTS.

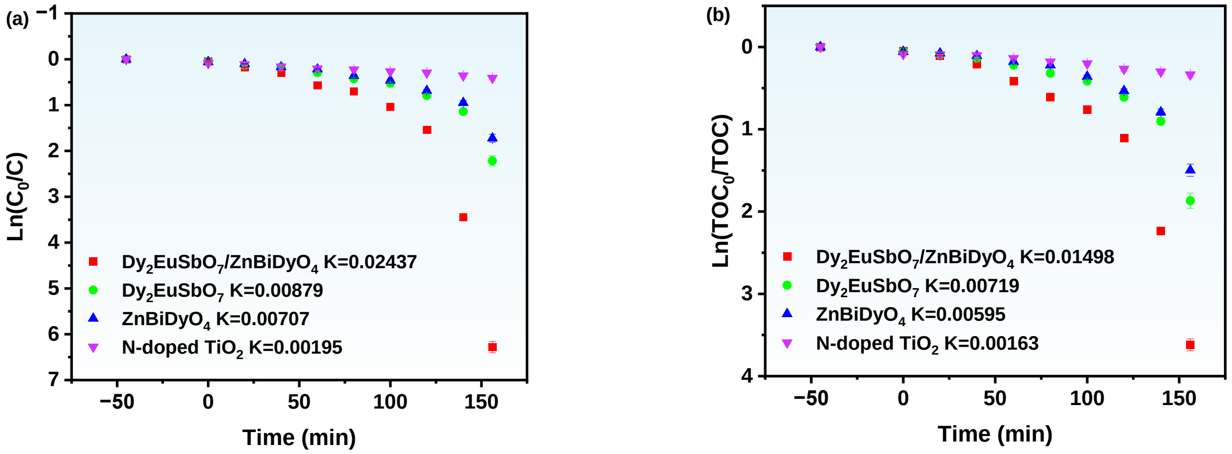

Figure 16. (**a**) Observed FOKT plots for the PTD of CPS with DZH as the photocatalyst or with Dy_2EuSbO_7 as the photocatalyst or with $ZnBiDyO_4$ or with N-doped TiO_2 as the photocatalyst under VSLID. (**b**) Observed FOKT plots for TOC during PTD of CPS in pesticide wastewater DZH as the photocatalyst or with Dy_2EuSbO_7 as the photocatalyst or with $ZnBiDyO_4$ or with N-doped TiO_2 as the photocatalyst under VSLID.

From Figures 14 and 15, it could be concluded that after FCDTS, under VSLID, the removal rate of CPS by DZHP was reduced by 4.12%, and the removal rate of TOC was reduced by 4.07%. The degradation efficiencies in the aforementioned four cycles did not show significant differences, indicating that DZHP was highly stable.

Figure 16 illustrates the first-order kinetic (FOKT) plots for CPS PTD using various photocatalysts (DZHP, Dy_2EuSbO_7, $ZnBiDyO_4$, and N-doped TiO_2) under VSLID conditions. The kinetic constants k for DZHP, Dy_2EuSbO_7, $ZnBiDyO_4$, and N-doped TiO_2 were 0.02437 min^{-1}, 0.00879 min^{-1}, 0.00707 min^{-1}, and 0.00195 min^{-1}, respectively. The kinetic constants K for TOC concentration were 0.01489 min^{-1}, 0.00719 min^{-1}, 0.00595 min^{-1}, and 0.00163 min^{-1}, respectively. The K_{TOC} values for CPS degradation by the same catalyst were lower than the K_C values, indicating that there were intermediate products in the process of photodegradation. DZHP exhibited higher mineralization efficiency.

Figure 17 illustrates the FOKT curve for the four-cycle degradation of CPS under VSLID using DZH as the photocatalyst. The results indicate that the kinetic constants k were 0.01788 min^{-1}, 0.01536 min^{-1}, 0.01384 min^{-1}, and 0.01270 min^{-1}, respectively. In the four-cycle degradation experiments, the kinetic constants k for DZHP were 0.01331 min^{-1}, 0.01221 min^{-1}, 0.01124 min^{-1}, and 0.01047 min^{-1} for TOC. It was consistent with the FOKT.

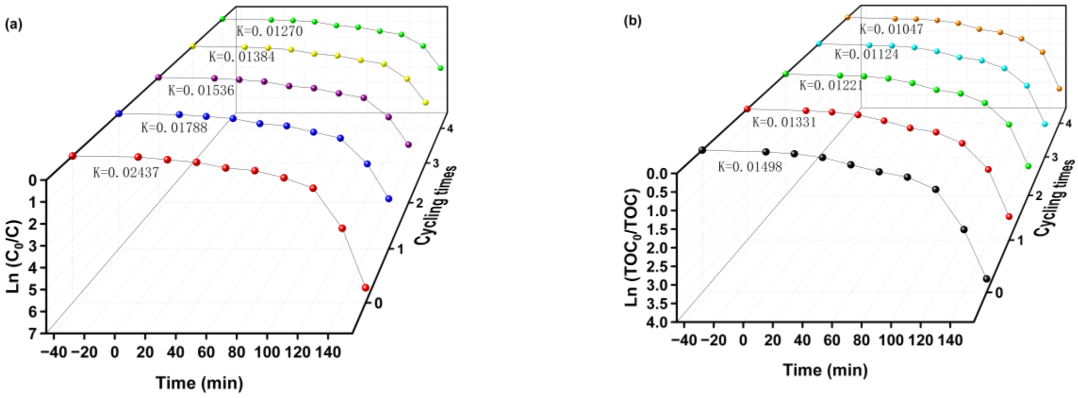

Figure 17. (**a**) Observed FOKT plots for the PTD of CPS with DZHP under VSLID for FCDTS. (**b**) The FCDTS of DZH as a photocatalyst for PTD of TOC in CPS under VSLID was observed.

Figure 18 illustrates the impact of various free radical scavengers, such as benzoquinone (BQ) isopropanol (IPA) or ethylenediamine tetraacetic acid (EDTA) on the removal of CPS by DZHP under VSLID conditions. Initially, at the onset of the photocatalytic experiment, different free radical scavengers were introduced into the CPS solution to identify the active species involved in its degradation. IPA was used to trap hydroxyl radicals (•OH), BQ to capture superoxide anions ($\bullet O_2^-$), and EDTA to bind to h^+. The concentration of IPA, BQ, or EDTA was set at 0.15 mmol L^{-1}, and the dosage was 1 mL. As depicted in Figure 19, the addition of BQ, IPA, or EDTA to the CPS solution reduced the removal rate by 44.22%, 35.68%, and 25.90%, respectively, compared to the control group. Hence, •OH, h^+ and $\bullet O_2^-$ were all active free radicals during CPS degradation. Figure 19 indicates that under VSLID conditions, •OH dominated in the CPS solution when DZHP was used as a photocatalyst for CPS degradation. Experiments with added scavengers revealed that •OH were more effective at oxidatively removing CPS from pesticide wastewater than $\bullet O_2^-$ or h^+. The order of scavengers' effectiveness in oxidatively removing CPS was $\bullet O_2^- > \bullet OH > h^+$.

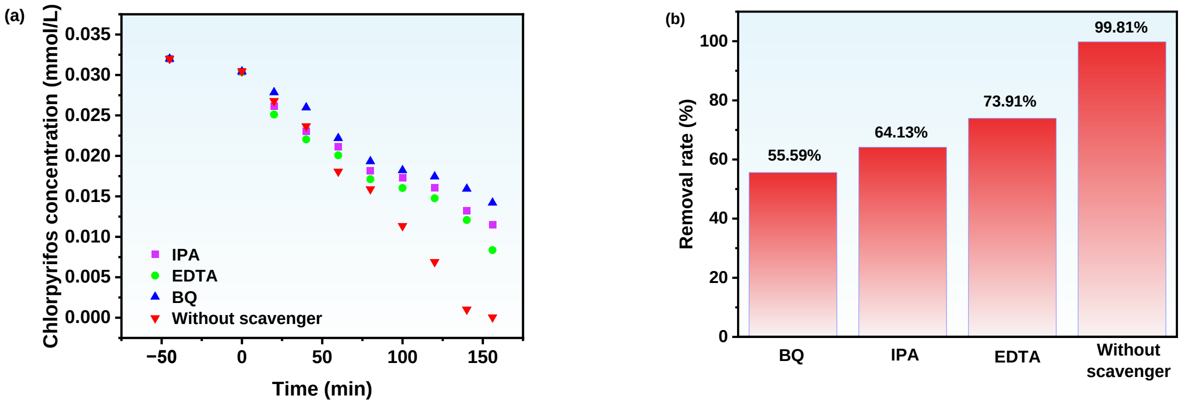

Figure 18. (**a**) Effect of different radical scavengers on removal efficiency of CPS with DZH as the photocatalyst under VSLID; (**b**) effect of different radical scavengers on removal rate of CPS with DZH as the photocatalyst under VSLID.

We used electron paramagnetic resonance (EPR) studies to look into the production of $\bullet O_2^-$ and •OH free radicals during the PDP process [95]. Figure 19 shows the EPR spectra of DMPO$\bullet O_2^-$ and DMPO•OH with DZHP as the photocatalyst. After 10 min of visible light exposure, a significant DMPO$\bullet O_2^-$ signal appeared, with four peaks in a 1:1:1:1 ratio, indicating $\bullet O_2^-$ radicals. The spectra likewise showed a four-line DMPO•OH signal in a 1:2:2:1 ratio after light exposure, suggesting the generation of

•OH radicals. A higher radical production was indicated by these signals' higher relative intensities, with $\bullet O_2^-$ yield being higher than •OH. These results align with previous free radical scavenger experiments.

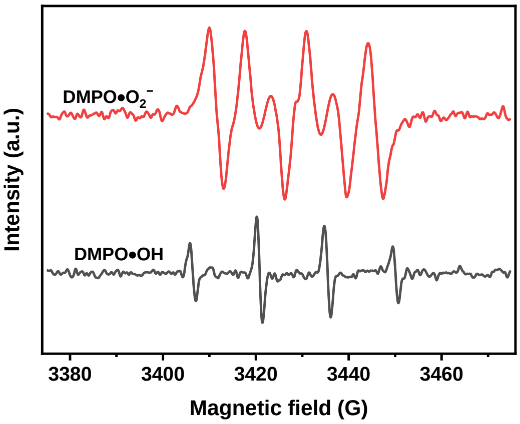

Figure 19. EPR spectrum for $DMPO\bullet O_2^-$ and DMPO•OH over DZHP.

The Photoluminescence (PL) spectrum and Time-Resolved Photoluminescence (TRPL) spectra of Dy_2EuSbO_7, $ZnBiDyO_4$, and DZHP are depicted in Figures 20 and 21a–c. Figure 20 shows the PL spectra of prepared Dy_2EuSbO_7 catalyst, the $ZnBiDyO_4$ catalyst, and the constructed DZHP. All samples showed an emission peak at 470 nm. With the lowest emission peak intensity and hence the lowest e^- and h^+ recombination rate, the DZHP had the maximum catalytic activity. The TRPL spectra of Dy_2EuSbO_7, $ZnBiDyO_4$, and DZHP in Figure 21a–c were fitted by the following double-exponential decay Equation (3) [95]:

$$I(t) = I_0 + A_1 exp\left(-\frac{t}{\tau_1}\right) + A_2 exp\left(-\frac{t}{\tau_2}\right) \tag{3}$$

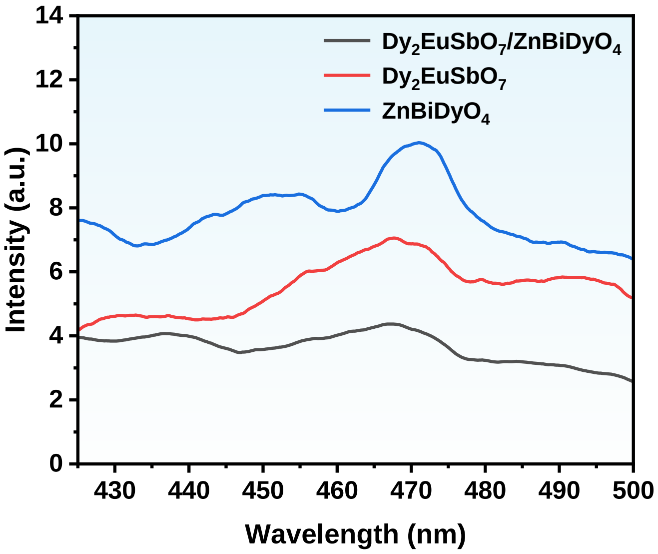

Figure 20. PL spectra of Dy_2EuSbO_7, $ZnBiDyO_4$, and the constructed DZHP.

In the provided equation, τ_1 and τ_2 represent the first and second-order decay times, and A_1 and A_2, were weighting coefficients of each decay channel [96]. DZHP (τ_1 = 1.37 ns, τ_2 = 1.26 ns, τ_{ave} = 1.25 ns) presented a much higher photogenerated charge carrier lifetime (PCC) than Dy_2EuSbO_7 (τ_1 = 1.61 ns, τ_2 = 1.21 ns, τ_{ave} = 1.21 ns) and $ZnBiDyO_4$ (τ_1 = 1.46 ns, τ_2 = 0.978 ns, τ_{ave} = 0.97 ns), which indicates that DZHP has the most excellent photocatalytic effect. To determine the average PCC lifetime (τ_{ave}), the following Equation (4) was utilized [97]:

$$\tau_{ave} = \left(A_1\tau_1^2 + A_2\tau_2^2\right)/(A_1\tau_1 + A_2\tau_2) \quad (4)$$

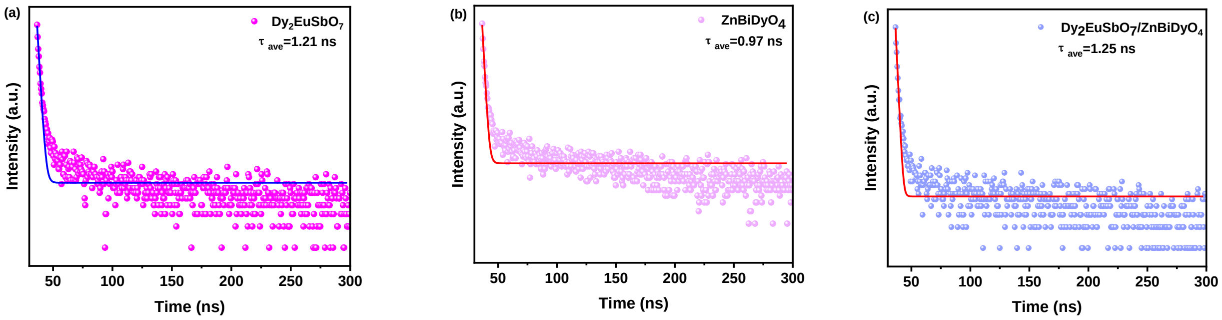

Figure 21. TRPL spectra of (**a**) Dy_2EuSbO_7, (**b**) $ZnBiDyO_4$, and (**c**) DZHP.

This study investigated the impact of prepared samples on the separation efficiency of PCC using photocurrent and electrochemical impedance spectroscopy (EIS). Figure 22a illustrates the transient photocurrent responses of DZHP, as well as individual samples of Dy_2EuSbO_7 and $ZnBiDyO_4$. The findings reveal that DZHP exhibited the highest photocurrent response intensity compared to Dy_2EuSbO_7 and $ZnBiDyO_4$. The effective diffusion of photoexcited e^- and the quick transfer of photoexcited h^+ across $ZnBiDyO_4$'s surface may be the causes of this increased photocurrent responsiveness. This phenomenon was facilitated by the potential difference existing between the valence bands of Dy_2EuSbO_7 and $ZnBiDyO_4$ within the DZHP composites. Consequently, the heightened photocurrent response in DZHP indicates that PCC was effectively separated during photodegradation, thereby extending its lifespan. These observations further elucidate the superior photocatalytic efficiency achieved by DZHP [98,99].

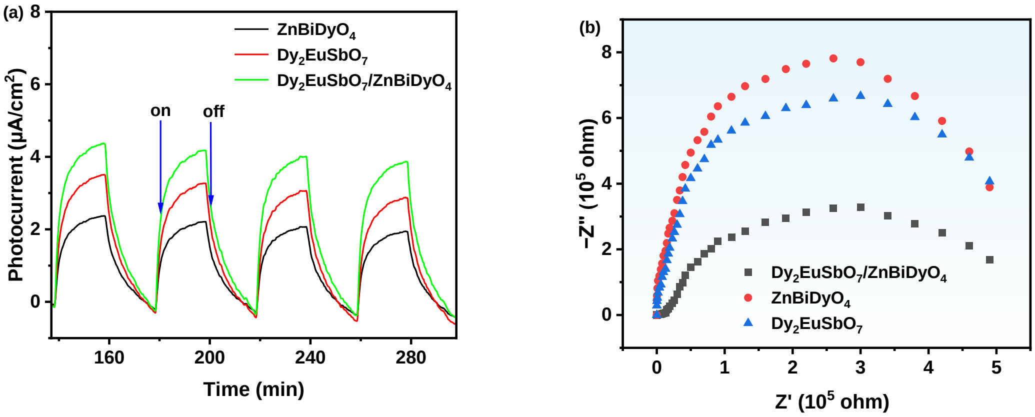

Figure 22. (**a**) Transient photocurrent and (**b**) Nyquist impedance plots of DZHP, Dy_2EuSbO_7, and $ZnBiDyO_4$.

EIS serves as another critical characterization of the migration process of photogenerated e^- and h^+ at the solid/electrolyte interface. The smaller the arc radius is, the higher the transmission efficiency of photogenerated e^- and h^+ is. Figure 22b illustrates the corresponding EIS diagrams for the prepared DZHP, Dy_2EuSbO_7, and $ZnBiDyO_4$ photocatalysts. The figure reveals that the arc radius sequence was $ZnBiDyO_4 > Dy_2EuSbO_7 >$ DZHP. These findings suggest that the prepared DZHP exhibited a more efficient separation of photogenerated e^- and h^+, along with a faster interfacial charge transfer.

2.7. Analysis of Possible Photocatalytic Degradation Mechanisms

Figure 23 displays the ultraviolet photoelectron spectroscopy (UPS) spectra of Dy_2EuSbO_7 and $ZnBiDyO_4$. The ionization potentials of Dy_2EuSbO_7 and $ZnBiDyO_4$ were determined using UPS. The onset (Ei) and cutoff (Ecutoff) binding energies for the two semiconductor samples are presented in Figure 23. The measured values for Dy_2EuSbO_7 and $ZnBiDyO_4$ were 1.523 eV and 17.175 eV, respectively, while the values for $ZnBiDyO_4$ were 0.124 eV and 17.625 eV, respectively. By calculating the excitation energy (approximately 21.2 eV), the ionization potentials of Dy_2EuSbO_7 and $ZnBiDyO_4$ were determined to be 2.791 eV and 1.217 eV, respectively [100]. The results indicate that the CB potentials of Dy_2EuSbO_7 and $ZnBiDyO_4$ were 0.111 eV and −0.563 eV, respectively. These results further validate the mechanism model proposed in this study.

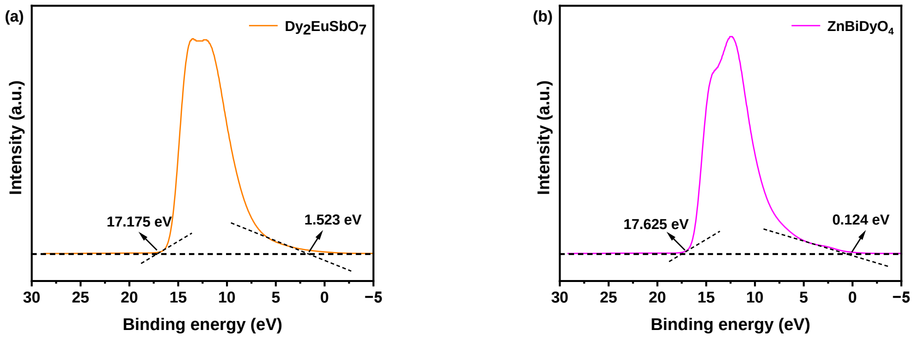

Figure 23. UPS spectra of (**a**) Dy_2EuSbO_7 and (**b**) $ZnBiDyO_4$ (the intersections of the black dash lines are indicated by the black arrows, representing the onset (Ei) and cutoff (Ecutoff) binding energy).

Figure 24 shows the possible PTD mechanism of CPS and DZHP under VSLID. It could be found that when the DZHP was irradiated with visible light, both Dy_2EuSbO_7 and $ZnBiDyO_4$ could absorb visible light and generated e^--h^+ pairs internally. Due to the CB of the $ZnBiDyO_4$ redox potential position (−0.563 eV) than Dy_2EuSbO_7 (0.111 eV) being more negative, light-induced e^- on the CB of $ZnBiDyO_4$ could be transferred to the CB of Dy_2EuSbO_7. The redox potential position of VB of Dy_2EuSbO_7 (2.791 eV) was more correct than that of VB of $ZnBiDyO_4$ (1.217 eV), and light-induced h^+ on Dy_2EuSbO_7 VB could be transferred to VB of $ZnBiDyO_4$. Therefore, the coupling of Dy_2EuSbO_7 and $ZnBiDyO_4$ to produce DZHP could effectively reduce the recombination rate of photogenerated e^- and photogenerated h^+, thereby reducing the internal resistance, prolonging the lifetime of photogenerated e^- and photogenerated h^+, and improving the interfacial charge transfer efficiency [101]. Therefore, more oxidized radicals, such as •OH or $\bullet O_2^-$, could be produced to improve the degradation efficiency of CPS. In addition, the CB potential of $ZnBiDyO_4$ was −0.563 eV, which was greater than the negative value of $O_2/\bullet O_2^-$ (−0.33 eV vs. NHE), indicated that e^- within the CB of $ZnBiDyO_4$ could absorb oxygen to produce O, thereby degrading CPS (as shown in path ① in Figure 24). At the same time, the VB potential of Dy_2EuSbO_7 was 2.791 eV, which was corrected for $OH^-/\bullet OH$ (2.38 eV vs. NHE), indicated that the VB h^+ of Dy_2EuSbO_7 could oxidize H_2O or OH^- to •OH to degrade CPS, as shown in path ②. Finally, the light-induced h^+ in VB of $ZnBiDyO_4$ or Dy_2EuSbO_7 could directly oxidize CPS and degrade CPS due to their strong oxidizing capacity, which is shown as path ③. In summary, the excellent photocatalytic activity of DZHP for CPS degradation was mainly attributed to the efficient e^--h^+ separation induced by DZHP.

LC-MS was used to identify the intermediate products produced during the CPS degradation process in order to investigate the degradation mechanism of CPS. The intermediate products which were obtained during the PTD of CPS were identified as $C_7H_7Cl_3NO_3PS$ (m/z = 322), $C_5H_3Cl_3NO_3PS$ (m/z = 294), $C_5H_2Cl_3NO$ (m/z = 198), $C_9H_{11}Cl_3NO_4P$ (m/z = 334), and $C_7H_7Cl_3NO_4P$ (m/z = 306). Based on the detected intermediate products, the PTD pathway of CPS was proposed. Figure 25 shows the suggested PTD pathway scheme of CPS under VSLID with DZH as the photocatalyst. Figure 25 shows that oxidation and hydroxylation reactions occurred during the PTD of CPS. Ultimately, CPS was converted into CO_2 and water.

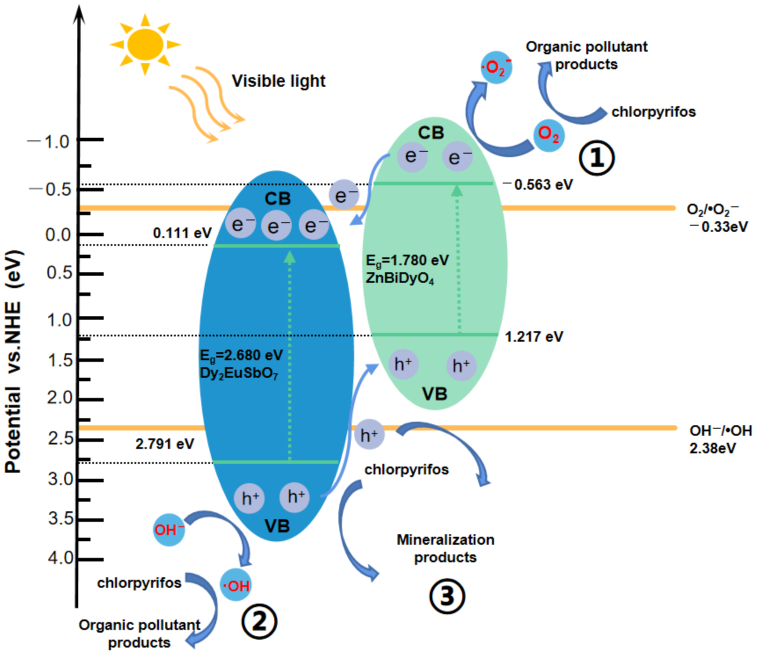

Figure 24. Possible PTD mechanism of CPS with DZH as the photocatalyst under VSLID.

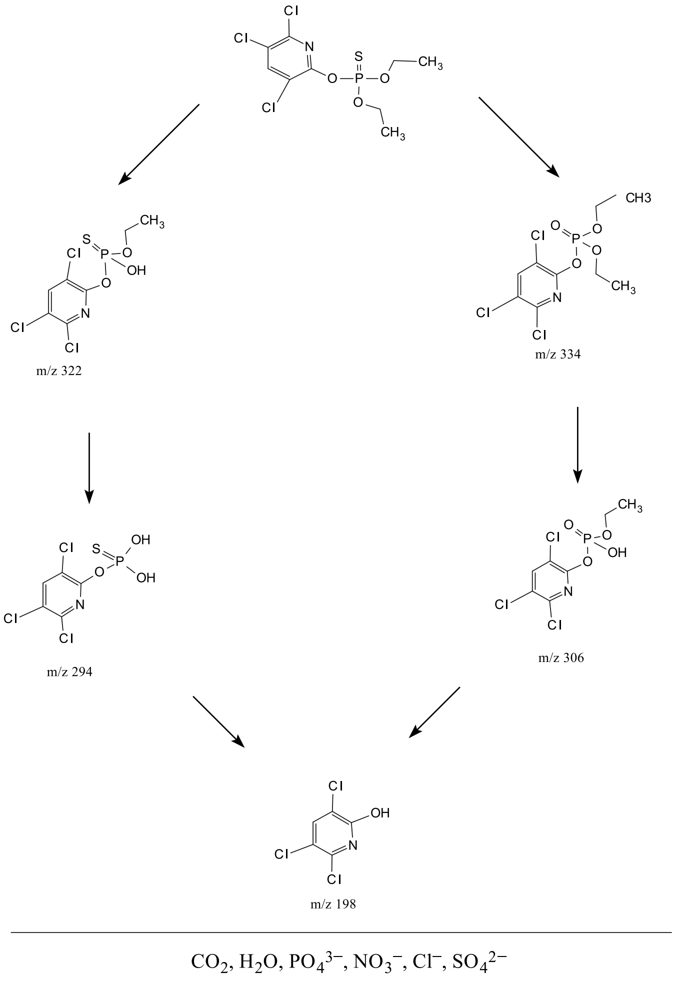

Figure 25. Suggested PTD pathway scheme for CPS under VSLID with DZH as photocatalyst.

3. Experimental Section

3.1. Materials and Reagents

In this study, Dy_2O_3 (purity 99.99%), Eu_2O_3 (purity 99.99%), Sb_2O_5 (purity 99.99%), Bi_2O_3 (purity 99.99%), ZnO (purity 99.99%), Ethylenediaminetetraacetic acid (purity of 99.5%), Isopropyl alcohol (purity greater than 99.7%), P-benzoquinone (purity greater than 98.0%), anhydrous ethanol (purity greater than 99.5%), chlorpyrifos (purity greater than 99.0%), and Ultra-pure water (18.25 MU cm) were used. All chemicals were purchased from Sinopharm Group Chemical Reagent Co., Ltd. (Shanghai, China) or Aladdin Group Chemical Reagent Co., Ltd. (Shanghai, China) or Tianjin Bodi Chemical Co., Ltd. (Tianjin, China) and were of analytical grade or gas chromatography grade.

3.2. Preparation Method of Dy_2EuSbO_7

Dy_2EuSbO_7 was synthesized via the HTSSM.

(1) We mixed the Dy_2O_3 powder, Eu_2O_3 powder and Sb_2O_5 powder evenly at a molar ratio of Dy_2O_3:Eu_2O_3:Sb_2O_5 = 2:1:1, then added them into a ball mill and grind for 120 min to obtain the powder.

(2) We put the above powder into an oven and heat it at 180 °C for 180 min. After drying, we pressed the powder into a sheet and placed it in an alumina crucible. Then, the alumina crucible containing the powder was placed in a high-temperature sintering furnace (HTSF) and sintered at room temperature (RT) to 450 °C in the range of 9.5 °C/min and then held at 450 °C for 5 h. Then, the temperature was raised to 700 °C in the range of 8.5 °C/min and kept at 700 °C for 14 h. Then, the temperature was raised to 1050 °C in the range of 7.5 °C/min and kept at 1050 °C for 32 h. Finally, the temperature was lowered from 1050 °C to RT at a cooling rate of 6.3 °C/min, resulting in the first sintered tablet.

(3) After the chamber of the HTSF was cooled to RT, the alumina crucible was removed from the chamber of the HTSF. Then, we removed the sample-pressed sheet from the alumina crucible after the first sintering, and we put it into an agate mortar for crushing and grinding for 60 min. We put the ground powder into an alumina crucible, pressing it into a sheet, and then placed the alumina crucible containing the sample-pressed sheet into a HTSF for a second sintering. The temperature was raised from RT to 550 °C in the range of 9.6 °C/min and then held at 550 °C for 5 h. Then, the temperature was raised to 1000 °C in the range of 8.2 °C/min and kept at 1000 °C for 16 h. Then, the temperature was raised to 1150 °C in the range of 7.2 °C/min and kept at 1150 °C for 26 h. Finally, the temperature was lowered from 1150 °C to RT at a cooling rate of 6.1 °C/min to obtain the second sintered tablet.

(4) After the chamber of the HTSF was cooled to RT, the alumina crucible was removed from the chamber of the HTSF. Then, we removed the sample pressed from the second sintering in the alumina crucible, and we put it into an agate mortar for crushing and grinding for 80 min. We put the ground powder into an alumina crucible, and then we pressed it into a sheet to obtain a sample-pressed sheet. Then, the alumina crucible containing the sample-pressed sheet was placed in a HTSF for a third sintering. The temperature was raised to 700 °C at RT in the range of 8.8 °C/min and held at 700 °C for 7 h. Then, the temperature was raised to 1100 °C in the range of 8.1 °C/min and kept at 1100 °C for 24 h. Then, the temperature was raised to 1300 °C in the range of 6.8 °C/min and held at 1300 °C for 42 h. Finally, the temperature was lowered from 1300 °C to RT at a cooling rate of 6.3 °C/min to obtain the third sintered tablet.

(5) After the chamber of the HTSF was cooled to RT, the alumina crucible was removed from the chamber of the HTSF. Then, we removed the sample pressed from the alumina crucible after the third sintering, and we put it into an agate mortar for crushing and grinding for 80 min. Finally, the Dy_2EuSbO_7 powder catalyst was obtained.

3.3. Preparation Method of $ZnBiDyO_4$

$ZnBiDyO_4$ was synthesized via the HTSSM.

(1) We mixed the Bi_2O_3 powder, Dy_2O_3 powder and ZnO powder evenly at a molar ratio of Bi_2O_3:Dy_2O_3:ZnO = 1.15:1:2, then added them into a ball mill and grind for 120 min to obtain the powder.

(2) We put the above powder into an oven and heated it at 180 °C for 180 min. After drying, we pressed the powder into a sheet and placed it in an alumina crucible. Then, the alumina crucible containing the powder was placed in a HTSF and sintered at RT to 450 °C in the range of 9.5 °C/min and then held at 450 °C for 5 h. Then, the temperature was raised to 700 °C in the range of 8.5 °C/min and kept at 700 °C for 14 h. Then, the temperature was raised to 1000 °C in the range of 7.5 °C/min and kept at 1000 °C for 32 h. Finally, the temperature was lowered from 1000 °C to RT at a cooling rate of 6.3 °C/min, resulting in the first sintered tablet.

(3) After the chamber of the HTSF was cooled to RT, the alumina crucible was removed from the chamber of the HTSF. Then, we removed the sample-pressed sheet from the alumina crucible after the first sintering, and we put it into an agate mortar for crushing and grinding for 60 min. We put the ground powder into an alumina crucible, pressing it into a sheet, and then place the alumina crucible containing the sample-pressed sheet into a HTSF for a second sintering. The temperature was raised from RT to 550 °C in the range of 9.6 °C/min and then held at 550 °C for 5 h. Then, the temperature was raised to 800 °C in the range of 8.2 °C/min and kept at 800 °C for 16 h. Then, the temperature was raised to 1100 °C in the range of 7.2 °C/min and kept at 1100 °C for 26 h. Finally, the temperature was lowered from 1100 °C to RT at a cooling rate of 6.1 °C/min to obtain the second sintered tablet.

(4) After the chamber of the HTSF was cooled to RT, the alumina crucible was removed from the chamber of the HTSF. Then, we removed the sample pressed from the second sintering in the alumina crucible, and we put it into an agate mortar for crushing and grinding for 80 min. We put the ground powder into an alumina crucible and then pressed it into a sheet to obtain a sample-pressed sheet. Then, the alumina crucible containing the sample-pressed sheet was placed in a HTSF for a third sintering. The temperature was raised to 600 °C at RT in the range of 8.8 °C/min and held at 600 °C for 7 h. Then, the temperature was raised to 1000 °C in the range of 8.1 °C/min and kept at 1000 °C for 24 h. Then, the temperature was raised to 1250 °C in the range of 6.8 °C/min and held at 1250 °C for 42 h. Finally, the temperature was lowered from 1250 °C to RT at a cooling rate of 6.3 °C/min to obtain the third sintered tablet.

(5) After the chamber of the HTSF was cooled to RT, the alumina crucible was removed from the chamber of the HTSF. Then, we removed the sample pressed from the alumina crucible after the third sintering, and we put it into an agate mortar for crushing and grinding for 80 min. Finally, the Zn_2BiDyO_4 powder catalyst was obtained.

3.4. Synthesis of N-Doped TiO_2

Using tetrabutyl titanate as a precursor and ethanol as a solvent, nitrogen-doped titanium dioxide (N-doped TiO_2) catalysts were successfully prepared by the sol-gel method. The specific preparation process is as follows:

Firstly, we thoroughly mixed 17 mL of tetrabutyl titanate with 40 mL of anhydrous ethanol to form solution A. We mixed 40 mL anhydrous ethanol, 10 mL glacial acetic acid, and 5 mL double-distilled water evenly to obtain solution B. Subsequently, under strong magnetic stirring, solution A was added dropwise to solution B to form a transparent and uniform colloidal suspension.

Subsequently, under the condition of magnetic stirring, ammonia water with a N/Ti ratio precisely controlled at 8 mol% was added to the transparent colloid suspension and stirred continuously for 1 h. After this step, the colloidal suspension was aged for 2 days to form a stable dry gel.

After that, the obtained dry gel was ground into powder and calcined at 500 °C for 2 h. After the calcination was completed, the calcined products were further ground in an agate mortar and finely screened through a vibrating screen to obtain N-doped TiO_2 (NT) powder with uniform particle size and high purity.

3.5. Synthesis of Dy_2EuSbO_7/$ZnBiDyO_4$ Heterojunction Photocatalysts

DZHP was synthesized via the HTSSM.

(1) We mixed the Dy_2EuSbO_7 powder and the $ZnBiDyO_4$ powder evenly at a molar ratio of 1:1, then added them into a ball mill and grind for 120 min to obtain the powder.

(2) We put the above powder into an oven and heat it at 180 °C for 180 min. After drying, we pressed the powder into a sheet and placed it in an alumina crucible. Then, the alumina crucible containing the powder was placed in a HTSF and sintered at RT to 350 °C in the range of 9.5 °C/min and then held at 350 °C for 5 h. Then, the temperature was raised to 700 °C in the range of 8.5 °C/min and kept at 700 °C for 14 h. Then, the temperature was raised to 900 °C in the range of 7.5 °C/min and kept at 900 °C for 32 h. Finally, the temperature was lowered from 900 °C to RT at a cooling rate of 6.3 °C/min, resulting in the first sintered tablet.

(3) After the chamber of the HTSF was cooled to RT, the alumina crucible was removed from the chamber of the HTSF. Then, we removed the sample pressed sheet from the alumina crucible after the first sintering and put it into an agate mortar for crushing and grinding for 60 min. We put the ground powder into an alumina crucible, pressing it into a sheet, and then placed the alumina crucible containing the sample pressed sheet into a HTSF for a second sintering. The temperature was raised from RT to 350 °C in the range of 9.6 °C/min and then held at 350 °C for 5 h. Then, the temperature was raised to 800 °C in the range of 8.2 °C/min and kept at 800 °C for 16 h. Then, the temperature was raised to 1000 °C in the range of 7.2 °C/min and kept at 1000 °C for 26 h. Finally, the temperature was lowered from 1000 °C to RT at a cooling rate of 6.1 °C/min to obtain the second sintered tablet.

(4) After the chamber of the HTSF was cooled to RT, the alumina crucible was removed from the chamber of the HTSF. Then, we removed the sample-pressed from the second sintering in the alumina crucible and put it into an agate mortar for crushing and grinding for 80 min. We put the ground powder into an alumina crucible, and then we pressed it into a sheet to obtain a sample-pressed sheet. Then, the alumina crucible containing the sample-pressed sheet was placed in a HTSF for a third sintering. The temperature was raised to 500 °C at RT in the range of 8.8 °C/min and held at 500 °C for 7 h. Then, the temperature was raised to 900 °C in the range of 8.1 °C/min and kept at 900 °C for 24 h. Then, the temperature was raised to 1100 °C in the range of 6.8 °C/min and held at 1100 °C for 42 h. Finally, the temperature was lowered from 1100 °C to RT at a cooling rate of 6.3 °C/min to obtain the third sintered tablet.

(5) After the chamber of the HTSF was cooled to RT, the alumina crucible was removed from the chamber of the HTSF. Then, we removed the sample pressed from the alumina crucible after the third sintering, and we put it into an agate mortar for crushing and grinding for 80 min. Finally, the DZHP material was obtained.

3.6. Characterizations

We conducted an in-depth analysis of the crystal structures of Dy_2EuSbO_7 and $ZnBiDyO_4$ using X-ray diffractometer (XRD, Shimadzu, XRD-6000, Cu Kα radiation, λ = 1.54184 Å, sampling pitch of 0.02°, preset time of 0.3 s step-1, Kyoto, Japan). In order to further reveal the conformational and microstructural characteristics of DZHP, we characterized it using a transmission electron microscope (TEM, Talos F200X G2, Thermo Fisher Scientific, Waltham, MA, USA) and determined its constituent elements using energy dispersive spectroscopy (EDS). In order to accurately obtain Dy_2EuSbO_7, we tested the band width information of $ZnBiDyO_4$ and DZHP using an UV-Vis spectrophotometer (UV-Vis DRS, Shimadzu, UV-3600, Kyoto, Japan). To clarify the functional groups and chemical bond types present in DZHP, we utilized a Fourier infrared spectrometer (FTIR, WQF-530A, Beifen-Ruili Analytical Instrument (Group) Co., Ltd., Beijing, China) to obtain the FTIR spectral data of Dy_2EuSbO_7 and $ZnBiDyO_4$. In addition, to reveal DZHP, we used a Raman spectrometer (INVIA0919-06, RENISHAW plx, Wotton-under-Edge, Gloucestershire GL 12 8JR, UK) to test the interaction relationships between various chemical bonds in Dy_2EuSbO_7 and $ZnBiDyO_4$. In order to have a comprehensive understanding of DZHP, we conducted a detailed analysis of the surface chemical composition and valence state information of Dy_2EuSbO_7 and $ZnBiDyO_4$ using an X-ray photoelectron spectrograph (XPS, PHI 5000 VersaProbe, UlVAC-PHI, Maoqi city, Japan) with an Al-kα X-ray source. To determine the ionization potentials of Dy_2EuSbO_7 and $ZnBiDyO_4$, we conducted relevant measurements using ultraviolet photo-electron spectroscopy (UPS, Escalab 250 xi, Thermo Fisher Scientific, Waltham, MA, USA). The related information about the free radicals in the samples was detected using an electron paramagnetic resonance spectrometer (EPR, A300, Bruker Corporation, Karlsruhe, Germany). The characteristics of PL and TRPL were analyzed using a fluorescence spectrophotometer (FLS980, Edinburgh Instruments Ltd., Edinburgh, UK).

3.7. Photoelectrochemical Experiments

The electrochemical impedance spectroscopy (EIS) experiment was conducted at the CHI660D electrochemical station (Chenhua Instruments Co., Shanghai, China). The experiment used a standard three-electrode system, with a prepared catalyst for the working electrode, a platinum plate for the counter electrode, and an Ag/AgCl electrode for the reference electrode. A 0.5 mol/L Na_2SO_4 aqueous solution was selected as the electrolyte for the experiment, and a 500 W Xe lamp equipped with a UV cut-off filter was used as the visible light source. When preparing the working electrode, the sample was mixed with chitosan and dissolved in dimethylformamide. After ultrasonic treatment, a uniform suspension was obtained, which was dropped onto ITO conductive glass and dried at a constant temperature of 80 °C for 10 min.

3.8. Experimental Setup and Procedure

This experiment was conducted in the photocatalytic reactor (XPA-7, Xujiang Electromechanical Plant, Nanjing, China). The experiment was conducted at a constant temperature of 20 °C, and the temperature was controlled through a circulating cooling water system to avoid temperature changes interfering with the results. We used a 500 W xenon lamp equipped with a 420 nm cut-off filter to simulate sunlight, ensuring the stability and accuracy of the light source. We used 12 quartz tubes of the same specification as reaction vessels, and each tube contained 40 mL of reaction solution, totaling 480 mL. Dy_2EuSbO_7 $ZnBiDyO_4$, and DZHP were used as photocatalysts with a unified dosage of 0.75 g/L. We introduced CPS with a concentration of 0.025 mmol/L to simulate actual pesticide wastewater treatment conditions. We regularly extracted suspension samples and filtered them with a 0.22 μm PES membrane to remove catalyst particles. We analyzed organic pollutants in the filtered solution using Agilent 200 high-performance liquid chromatography (Santa Clara, CA, USA). The mobile phase was a mixed solution of 50% CH3CN and 50% distilled deionized water. Before the photodegradation reaction, magnetic stirring was performed in the dark for 45 min to allow the photocatalyst to CPS and atmospheric oxygen reach adsorption/desorption equilibrium. Then, under visible light irradiation, we stirred the suspension at a speed of 500 rpm.

This article used a TOC analyzer (TOC-5000 A, Shimadzu Corporation, Kyoto, Japan) to measure CPS mineralization experimental data. We used potassium phthalate or anhydrous sodium carbonate as standard reagents to detect the concentration of TOC during PTD. We prepared standard solutions with multiple concentration gradients (0–100 mg/L) for calibrating the TOC analyzer. Six samples of 45 mL reaction solution were used to measure the TOC concentrations in each experiment to understand the changes in TOC concentration during PTD.

This study used advanced liquid chromatography–mass spectrometry (LC-MS, Thermo Quest LCQ Duo, Thermo Fisher Scientific Corporation, Waltham, MA, USA. Beta Basic-C18

HPLC column: 150 × 2.1 mm, ID of 5 μm, Thermo Fisher Scientific Corporation, Waltham, MA, USA) to analyze CPS and its degradation products. Here, the 20 μL solution obtained from the photocatalytic reaction was automatically injected into the system, with a mobile phase of 60% methanol and 40% ultrapure water, and a flow rate of 0.2 mL/min. The mass spectrometry analysis used the electric spray ionization interface. The capillary temperature, voltage, and spray voltage were set at 27 °C, 19.00 V, and 5000 V, respectively, and the sheath gas flow rate remained constant. Obtaining spectra in negative ion scanning mode, the m/z range was from 50 to 600.

The incident photon flux Io measured by a radiometer (Model FZ-A, Photoelectric Instrument Factory Beijing Normal University, Beijing, China) was determined to be 4.76×10^{-6} Einstein L^{-1} s^{-1} under VSLID.

4. Conclusions

For the first time, Dy_2EuSbO_7 and DZHP with high photocatalytic activity were synthesized using a HTSSM. The photophysical properties and photocatalytic performance were characterized using SEM-EDS, XRD, UV-vis, FTIR, Raman, and XPS techniques. The results revealed that Dy_2EuSbO_7 was a single phase with a pyrochlore structure and a cubic crystal system, categorized under the space group Fd3m. The lattice parameter and the band gap of Dy_2EuSbO_7 were a = 10.440423 Å and 2.680 eV, respectively. DZHP demonstrated high efficacy as a photocatalyst for the removal of CPS from wastewater, achieving CPS and TOC removal rates of 99.81% and 97.32%, respectively, after 156 min of visible light irradiation (VSLID). The CPS removal efficiency with DZHP as the photocatalyst was 1.12 times, 1.21 times, and 2.96 times greater than that with Dy_2EuSbO_7, $ZnBiDyO_4$, and N-doped TiO_2 catalysts, respectively, after 156 min of VSLID. Consequently, it could be inferred that DZHP is a highly effective photocatalyst for treating CPS-contaminated wastewater. Finally, potential photodegradation pathways for CPS were proposed.

Author Contributions: J.L.: conceptualization, data curation, formal analysis, investigation, methodology, software, visualization, writing—original draft preparation, writing—review and editing, validation. Y.X.: software, data curation, methodology, writing—original draft preparation, validation. L.H.: software, visualization, validation, methodology, software, validation, investigation. Y.Y.: formal analysis, investigation, writing—original draft preparation, validation, investigation. B.N.: software, visualization, validation, methodology, software, validation, investigation. G.Y.: formal analysis, methodology, writing—original draft preparation. Y.W.: formal analysis, methodology, writing—original draft preparation. All authors have read and agreed to the published version of the manuscript.

Funding: This study was supported by the Free Exploring Key Item of Natural Science Fundation of the Science and Technology Bureau of Jilin Province of China (Grant No. YDZJ202101ZYTS161).

Institutional Review Board Statement: Not applicable.

Informed Consent Statement: Not applicable.

Data Availability Statement: Data are contained within the article.

Conflicts of Interest: The authors declare no conflicts of interest.

References

1. Haq, M.T.; Sattar, M.A.; Hossain, M.M.; Hasan, M.M. Effects of fertilizers and pesticides on growth and yield of rice. *J. Biol. Sci.* **2002**, *2*, 84–88.
2. Bolognesi, C.; Merlo, F.D. Pesticides: Human health effects. *Encycl. Environ. Health* **2011**, *156*, 438–453.
3. Arias-Estévez, M.; López-Periago, E. The mobility and degradation of pesticides in soils and the pollution of groundwater resources. *Agric. Ecosyst. Env.* **2008**, *123*, 247–260. [CrossRef]
4. Malek, A. Environmental and occupational risk factors for amyotrophic lateral sclerosis: A case-control study. *Diss. Theses Gradworks* **2014**, *14*, 31–38. [CrossRef] [PubMed]
5. Kisby, G.E.; Muniz, J.F.; Scherer, J.; Lasarev, M.R.; Koshy, M.; Kow, Y.W. Biomarkers of oxidative stress and dna damage in agricultural workers. *J. Agromed.* **2009**, *14*, 206–214. [CrossRef]
6. Bortoli, S.; Coumoul, X. Impact des pesticides sur la santé humaine. *Prat. En. Nutr.* **2018**, *14*, 18–24. [CrossRef]

7. Betancourt, A.M.; Carr, R.L. The effect of chlorpyrifos and chlorpyrifos-oxon on brain cholinesterase, muscarinic receptor binding, and neurotrophin levels in rats following early postnatal exposure. *Toxicol. Sci.* **2004**, *77*, 63–71. [CrossRef]
8. Jinyan, W.; Huazhong, S.; Yuanqing, B.; Ninghui, S.; Yan, D.; Lichao, T. Effect of chlorpyrifos on enzyme activities and microbial activity in zijin mountain forest soil. *Asian J. Ecotoxicol.* **2017**, *12*, 210–218.
9. Supreeth, M.; Chandrashekar, M.A.; Sachin, N.; Raju, N.S. Effect of chlorpyrifos on soil microbial diversity and its biotransformation by *Streptomyces* sp. hp-11. *Biotech* **2016**, *6*, 147. [CrossRef]
10. Jafari, S.J.; Moussavi, G.; Hossaini, H. Degradation and mineralization of diazinon pesticide in UVC and UVC/TiO_2 process. *Desalin. Water Treat.* **2014**, *35*, 3782–3790.
11. Mirmasoomi, S.R.; Ghazi, M.M.; Galedari, M. Photocatalytic degradation of diazinon under visible light using TiO_2/Fe_2O_3 nanocomposite synthesized by ultrasonic-assisted impregnation method. *Sep. Purif. Technol.* **2017**, *175*, 418–427. [CrossRef]
12. Alam, M.W. Smart Poly(N-Isopropylacrylamide)-Based Microgels Supplemented with Nanomaterials for Catalytic Reduction Reactions—A Review. *Chemengineering* **2023**, *7*, 105. [CrossRef]
13. Ahmad, Z.; Tahir, R.; Sajjad, N.; Batool, F.; Zada, N.; Ullah, H. Cleansing Water: Harnessing Trimetallic Nanoparticles in Sunlight to Degrade Methylene Blue Dye, Aiding Aquatic Contaminant Cleanup. *Water* **2023**, *15*, 3404. [CrossRef]
14. Kanmoni, V.G.G.; Daniel, S.; Raj, G.A.G. Photocatalytic degradation of chlorpyrifos in aqueous suspensions using nanocrystals of ZnO and TiO_2. *React. Kinet. Mech. Catal.* **2012**, *106*, 325–339. [CrossRef]
15. Lee, D.E.; Kim, M.K.; Danish, M.; Jo, W.K. State-of-the-art review on photocatalysis for efficient wastewater treatment: Attractive approach in photocatalyst design and parameters affecting the photocatalytic degradation. *Catal. Commun.* **2023**, *183*, 106764. [CrossRef]
16. Liang, R.; Wu, H.; Hu, Z.; Sun, J.; Fu, C.; Li, S.; Zhang, X.; Zhou, M. Novel Photoelectrocatalytic System of Oxygen Vacancy-Rich Black TiO_{2-x} Nanocones Photoanode and Natural Air Diffusion Cathode for Efficient Water Purification and Simultaneous H_2O_2 Production. *Appl. Catal. B* **2024**, *352*, 124042. [CrossRef]
17. Bibi, S.; Shah, S.; Muhammad, F.; Siddiq, M.; Kiran, L.; Aldossari, S.; Sheikh, M.; Sarwar, S. Cu-Doped Mesoporous TiO_2 Photocatalyst for Efficient Degradation of Organic Dye via Visible Light Photocatalysis. *Chemosphere* **2023**, *339*, 139583. [CrossRef]
18. Liu, Z.J.; Zhang, Y.T.; Lee, J.; Xing, L. A review of application mechanism and research progress of Fe/montmorillonite-based catalysts in heterogeneous Fenton reactions. *J. Environ. Chem. Eng.* **2024**, *12*, 112152. [CrossRef]
19. Wang, J.L.; Tang, J.T. Fe-based Fenton-like catalysts for water treatment: Catalytic mechanisms and applications. *J. Mol. Liq.* **2021**, *332*, 115755. [CrossRef]
20. Chen, Z.; Chen, Q.; Li, D.; Zhong, Y.; Chen, H.; Peng, W. Metal Hydroxide-Catalyzed Heavy Oil Upgrading in Supercritical Water: Deuterium Tracing Study. *Energy Fuels* **2024**, *38*, 5738–5750. [CrossRef]
21. Zhang, L.; Zhang, J.; Li, H.; Feng, J.; Tian, X. Kinetics and hydrothermal combustion characteristics of ethanol in supercritical water. *J. Supercrit. Fluids* **2024**, *210*, 106291. [CrossRef]
22. Luo, C.; Teng, S.; Wang, J.; Xi, H. Energy yield from wastewater by supercritical water oxidation process: Experimental validation and simulation from the viewpoint of energy system. *Energy Convers. Manag.* **2024**, *299*, 117876. [CrossRef]
23. Chen, Z.; Zheng, Z.; He, C.; Liu, J.; Zhang, R.; Chen, Q. Oily sludge treatment in subcritical and supercritical water: A review. *J. Hazard. Mater.* **2022**, *433*, 128761. [CrossRef] [PubMed]
24. Fadaei, A.; Kargar, M. Photocatalytic degradation of chlorpyrifos in water using titanium dioxide and zinc oxide. *Fresenius Environ. Bull.* **2014**, *22*, 2442–2447.
25. Dalrymple, O.K.; Yeh, D.H.; Trotz, M.A. Removing pharmaceuticals and endocrine-disrupting compounds from wastewater by photocatalysis. *J. Chem. Technol. Biot.* **2007**, *82*, 121–134. [CrossRef]
26. Orbeci, C.; Totu, M.; Tanczos, S.K.; Vasile, E.; Dinu, A.; Nechifor, A.C. Preparation and properties of a photocatalyst with TiO_2 nanoparticles. *Optoelectron. Adv. Mat.* **2013**, *7*, 822–827.
27. Cao, G.S.; Wang, G.L.; Bai, Y.J.; Liu, M.X. Photocatalytic removal of Rhodamine B using Fe_3O_4/BiOBr magnetic microsphere under visible-light irradiation. *Micro Nano Lett.* **2015**, *10*, 115–118. [CrossRef]
28. Mashuri, S.I.S.; Ibrahim, M.L.; Kasim, M.F.; Mastuli, M.S.; Rashid, U.; Abdullah, A.H.; Islam, A.; Mijan, N.A.; Tan, Y.H.; Mansir, N.; et al. Photocatalysis for Organic Wastewater Treatment: From the Basis to Current Challenges for Society. *Catalysts* **2020**, *10*, 1260. [CrossRef]
29. Alam, M.W.; Khalid, N.R.; Naeem, S.; Niaz, N.A.; Ahmad Mir, T.; Nahvi, I.; Souayeh, B.; Zaidi, N. Novel Nd-N/TiO_2 Nanoparticles for Photocatalytic and Antioxidant Applications Using Hydrothermal Approach. *Materials* **2022**, *15*, 6658. [CrossRef]
30. Slimings, C.; Riley, V. Antibiotics and hospital-acquired Clostridium diffificile infection: Update of systematic review and meta-analysis. *J. Antimicrob. Chemother.* **2013**, *69*, 881–891. [CrossRef]
31. Klavarioti, M.; Mantzavinos, D.; Kassinos, D. Removal of residual pharmaceuticals from aqueous systems by advanced oxidation processes. *Environ. Int.* **2009**, *35*, 402–417. [CrossRef] [PubMed]
32. Alam, M.W.; Azam, H.; Khalid, N.R.; Naeem, S.; Hussain, M.K.; BaQais, A.; Farhan, M.; Souayeh, B.; Zaidi, N.; Khan, K. Enhanced Photocatalytic Performance of Ag_3PO_4/Mn-ZnO Nanocomposite for the Degradation of Tetracycline Hydrochloride. *Crystals* **2022**, *12*, 1156. [CrossRef]
33. Gaya, U.I.; Abdullah, A.H. Heterogeneous photocatalytic degradation of organic contaminants over titanium dioxide: A review of fundamentals. *J. Photochem. Photobiol. C Rev.* **2001**, *9*, 1–12. [CrossRef]

34. Lv, Y.C.; Tian, C.; Yan, A.; Liu, M.H. Preparation of Activated Carbon Supported Nano-TiO_2 Photocatalyst Material and Its Application in Papermaking Midcourse Wastewater. *Adv. Mater. Peocess.* **2011**, *311–313*, 1446–1450.
35. Shakil, M.; Inayat, U.; Khalid, N.R.; Tanveer, M.; Gillani, S.S.A.; Tariq, N.H.; Shah, A.; Mahmood, A.; Dahshan, A. Enhanced structural, optical, and photocatalytic activities of Cd–Co doped Zn ferrites for degrading methyl orange dye under irradiation by visible light. *J. Phys. Chem. Solids* **2021**, *161*, 110419. [CrossRef]
36. Koci, K.; Krejcikova, S.; Solcova, O.; Obalova, L. Photocatalytic decomposition of N_2O on Ag-TiO_2. *Catal. Today* **2012**, *191*, 134–137. [CrossRef]
37. Naddafi, K.; Nabizadeh, R.; Silva-Martinez, S.; Shahtaheri, S.J.; Yaghmaeian, K.; Badiei, A.; Amiri, H. Modeling of Chlorpyrifos degradation by TiO_2 photo catalysis under visible light using response surface methodology. *Desalin. Water Treat.* **2018**, *106*, 220–225. [CrossRef]
38. Tong, T.; Zhang, H.; Chen, J.G.; Jin, D.R.; Cheng, J.R. The photocatalysis of $BiFeO_3$ disks under visible light irradiation. *Catal. Commun.* **2016**, *87*, 23–26. [CrossRef]
39. Yang, J.; Zhong, H.Q.; Li, M.; Zhang, L.Z.; Zhang, Y.M. Markedly enhancing the visible-light photocatalytic activity of $LaFeO_3$ by post-treatment in molten salt. *React. Kinet. Catal. Lett.* **2009**, *97*, 269–274. [CrossRef]
40. Hu, C.Y.; Xu, J.; Zhu, Y.Q.; Chen, A.C.; Bian, Z.Y.; Wang, H. Morphological effect of $BiVO_4$ catalysts on degradation of aqueous paracetamol under visible light irradiation. *Environ. Sci. Pollut. Res.* **2016**, *23*, 18421–18428. [CrossRef]
41. Jothivenkatachalam, K.; Prabhu, S.; Nithya, A.; Mohan, S.C.; Jeganathan, K. Solar, visible and UV light photocatalytic activity of $CoWO_4$ for the decolourization of methyl orange. *Desalin. Water Treat.* **2015**, *54*, 3134–3145. [CrossRef]
42. Zhang, W.J.; Ma, Z.; Du, L.; Li, H. Role of PEG4000 in sol-gel synthesis of $Sm_2Ti_2O_7$ photocatalyst for enhanced activity. *J. Alloy. Compd.* **2017**, *704*, 26–31. [CrossRef]
43. Luan, J.F.; Hu, Z.T. Synthesis, Property Characterization, and Photocatalytic Activity of Novel Visible Light-Responsive Photocatalyst Fe_2BiSbO_7. *Int. J. Photoenergy* **2012**, *2012*, 301954. [CrossRef]
44. Luan, J.F.; Shen, Y.; Li, Y.Y.; Paz, Y. The Structural, Photocatalytic Property Characterization and Enhanced Photocatalytic Activities of Novel Photocatalysts Bi_2GaSbO_7 and Bi_2InSbO_7 during Visible Light Irradiation. *Materials* **2016**, *9*, 801. [CrossRef]
45. He, J.Y.; Yu, Q.; Zhou, Y.P.; Wang, Y.W.; Long, F. Rare Earth Ion Yb^{3+} Doping of Bi_2WO_6 with Excellent Visible-light Photocatalytic Activity. *J. Wuhan Univ. Technol.* **2020**, *35*, 348–355. [CrossRef]
46. Park, B.G. Photoluminescence and photocatalytic properties of Eu^{3+}-doped $CaZnTiO_3$ perovskites with metal ion loading. *Korean J. Chem. Eng.* **2019**, *36*, 613–619. [CrossRef]
47. Yang, X.; Gong, R.; Dong, Z.; Liu, G.; Han, Y.; Hou, Y.; Li, Y.; Guan, M.; Gong, X.; Tang, J. Polymeric Carbon Nitride-CNTs-Ferric Oxide All-Solid Z-Scheme Heterojunction with Improved Photocatalytic Activity towards Organic Dye Removal. *Catalysts* **2024**, *14*, 516. [CrossRef]
48. Lei, Z.D.; Wang, J.J.; Wang, L.; Yang, X.Y.; Xu, G.; Tang, L. Efficient photocatalytic degradation of ibuprofen in aqueous solution using novel visible-light responsive graphene quantum dot/$AgVO_3$ nanoribbons. *J. Hazard. Mater.* **2016**, *312*, 298–306. [CrossRef]
49. Wang, J.; Zhang, Q.; Deng, F.; Luo, X.B.; Dionysiou, D.D. Rapid toxicity elimination of organic pollutants by the photocatalysis of environment-friendly and magnetically recoverable step-scheme $SnFe2O_4$/$ZnFe_2O_4$ nano-heterojunctions. *Chem. Eng. J.* **2020**, *379*, 122264. [CrossRef]
50. Xia, C.; Wang, H.; Kim, J.K.; Wang, J. Rational design of metal oxide-based heterostructure for efficient photocatalytic and photoelectrochemical systems. *Adv. Funct. Mater.* **2021**, *31*, 2008247. [CrossRef]
51. Bao, N.; Li, Y.; Yu, X.H.; Niu, J.J.; Wu, G.L.; Xu, X.H. Removal of anionic azo dye from aqueous solution via an adsorption-photosensitized regeneration process on a TiO_2 surface. *Environ. Sci. Pollut. Res.* **2013**, *20*, 897–906. [CrossRef]
52. Lam, M.W.; Mabury, S.A. Photodegradation of the pharmaceuticals atorvastatin, carbamazepine, levofloxacin, and sulfamethoxazole in natural waters. *Aquat. Sci.* **2005**, *67*, 177–188. [CrossRef]
53. Dil, M.A.; Haghighatzadeh, A.; Mazinani, B. Photosensitization effect on visible-light-induced photocatalytic performance of TiO_2/chlorophyll and flavonoid nanostructures: Kinetic and isotherm studies. *Bull. Mater. Sci.* **2019**, *42*, 248. [CrossRef]
54. Lu, T.; Wu, L.S.; Liu, G.; Li, C.X.; He, T.Y.; Zhang, W.T. Progress on visible photocatalysis of BiOCl composite photocatalyst. *Appl. Chem. Indust.* **2018**, *47*, 2541–2546, 2549.
55. Li, G.; Yang, C.; He, Q.; Liu, J. Ag-based photocatalytic heterostructures: Construction and photocatalytic energy conversion application. *J. Environ. Chem. Eng.* **2022**, *10*, 107374. [CrossRef]
56. He, Q.B.; Hu, Z.; Ge, M. Research Progress on Photo—Degradation of Antibiotics in Water by BiOX (X = Cl, Br, I) Composite Photocatalytic Materials. *Chin. J. Appl. Chem.* **2021**, *38*, 754–766.
57. Lin, Y.; Yang, C.P.; Wu, S.H.; Li, X.; Chen, Y.J.; Yang, W.L. Construction of Built-In Electric Field within Silver Phosphate Photocatalyst for Enhanced Removal of Recalcitrant Organic Pollutants. *Adv. Funct. Mater.* **2020**, *30*, 2002918. [CrossRef]
58. Che, L.; Pan, J.; Cai, K.; Cong, Y.; Lv, S.W. The construction of p-n heterojunction for enhancing photocatalytic performance in environmental application: A review. *Sep. Purif. Technol.* **2023**, *315*, 123708. [CrossRef]
59. Cheng, L.; Chen, Q.; Li, J.; Liu, H. Boosting the photocatalytic activity of $CdLa_2S_4$ for hydrogen production using Ti_3C_2 MXene as a co-catalyst. *Appl. Catal. B Environ.* **2020**, *267*, 118379. [CrossRef]
60. Xu, X.L.; Song, W. Synthesis and photocatalytic activity of heterojunction $ZnFe_2O_4$-$BiVO_4$. *Mater. Technol.* **2017**, *32*, 472–479. [CrossRef]

61. Ma, C. Fabrication and characterization of NiOx/Bi_2WO_6 with enhanced photocatalytic activity under visible light illumination. *Adv. Mater. Res.* **2013**, *690–693*, 429–432. [CrossRef]
62. Jourshabani, M.; Shariatinia, Z.; Badiei, A. In situ fabrication of SnO_2/S-doped g-C_3N_4 nanocomposites and improved visible light driven photodegradation of methylene blue. *J. Mol. Liq.* **2017**, *248*, 688–702. [CrossRef]
63. Jourshabani, M.; Shariatinia, Z.; Badiei, A. High efficiency visible-light-driven Fe_2O_3 -xS(x)/S-doped g-C_3N_4 heterojunction photocatalysts: Direct Z-scheme mechanism. *J. Mater. Sci. Technol.* **2018**, *34*, 1511–1525. [CrossRef]
64. Rostami, M.; Sharafi, P.; Mozaffari, S.; Adib, K.; Sobhani-Nasab, A.; Rahimi-Nasrabadi, M.; Fasihi-Ramandi, M.; Ganjali, M.R.; Badiei, A. A facile preparation of $ZnFe_2O_4$-CuO-N/B/RGO and $ZnFe_2O_4$-CuO-C_3N_4 ternary heterojunction nanophotocatalyst: Characterization, biocompatibility, photo-Fenton-like degradation of MO and magnetic properties. *J. Mater. Sci. Mater. Electron.* **2021**, *32*, 5457–5472. [CrossRef]
65. Saeed, M.; Muneer, M.; Akram, N.; ul Haq, A.; Afzal, N.; Hamayun, M. Synthesis and characterization of silver loaded alumina and evaluation of its photo catalytic activity on photo degradation of methylene blue dye. *Chem. Eng. Res. Des.* **2019**, *148*, 218–226. [CrossRef]
66. Saeed, M.; Muneer, M.; Mumtaz, N.; Siddique, M.; Akram, N.; Hamayun, M. Ag-Co_3O_4: Synthesis, characterization and evaluation of its photo-catalytic activity towards degradation of rhodamine B dye in aqueous medium. *Chin. J. Chem. Eng.* **2018**, *26*, 1264–1269. [CrossRef]
67. Wang, J.H.; Zou, Z.G.; Ye, J.H. Synthesis, structure and photocatalytic property of a new hydrogen evolving photocatalyst Bi_2InTaO_7. *Mater. Sci. Forum* **2003**, *423–425*, 485–490. [CrossRef]
68. Kohno, M.; Ogura, S.; Sato, K.; Inoue, Y. Properties of photocatalysts with tunnel structures: Formation of a surface lattice O−radical by the UV irradiation of $BaTi_4O_9$ with a pentagonal-prism tunnel structure. *Chem. Phys. Lett.* **1997**, *267*, 72–76. [CrossRef]
69. Kato, H.; Nakagawa, S. Water Splitting into H_2 and O_2 on New $Sr_2M_2O_7$ (M = Nb and Ta) Photocatalysts with layered perovskite structures: Factors affecting the photocatalytic activity. *J. Phys. Chem. B* **2000**, *104*, 571–575.
70. Nowak, M.; Kauch, B.; Szperlich, P. Determination of energy band gap of nanocrystalline SbSI. *Rev. Sci. Instrum.* **2009**, *80*, 046107. [CrossRef]
71. Ji, L.; Chen, N.; Du, G.; Yan, M.; Shi, W. Synthesis and luminescence of Y2O3:Eu^{3+} inorganic—Organic hybrid nanostructures with thenoyltrifluoroacetone. *Ceram. Int.* **2014**, *40*, 3117–3122. [CrossRef]
72. Achehboune, M.; Khenfouch, M.; Boukhoubza, I.; Leontie, L.; Doroftei, C.; Carlescu, A.; Bulai, G.; Mothudi, B.; Zorkani, I.; Jorio, A. Microstructural, FTIR and Raman spectroscopic study of Rare earth doped ZnO nanostructures. *Mater. Today Proc.* **2022**, *53*, 319–323. [CrossRef]
73. Bosca, M.; Pop, L.; Borodi, G.; Pascuta, P.; Culea, E. XRD and FTIR structural investigations of erbium-doped bismuth–lead–silver glasses and glass ceramics. *J. Alloy. Compd.* **2009**, *479*, 579–582. [CrossRef]
74. Pascuta, P.; Culea, E. FTIR spectroscopic study of some bismuth germanate glasses containing gadolinium ions. *Mater. Lett.* **2008**, *62*, 4127–4129. [CrossRef]
75. Kaviyarasu, K.; Sajan, D.; Devarajan, P.A. A rapid and versatile method for solvothermal synthesis of Sb2O3 nanocrystals under mild conditions. *Appl. Nanosci.* **2012**, *3*, 529–533. [CrossRef]
76. Rada, S.; Rus, L.; Rada, M.; Zagrai, M.; Culea, E.; Rusu, T. Compositional dependence of structure, optical and electrochemical properties of antimony(III) oxide doped lead glasses and vitroceramics. *Ceram. Int.* **2014**, *40*, 15711–15716. [CrossRef]
77. Janani, B.; Okla, M.K.; Abdel-Maksoud, M.A.; AbdElgawad, H.; Thomas, A.M.; Raju, L.L.; Al-Qahtani, W.H.; Khan, S.S. CuO loaded ZnS nanoflower entrapped on PVA-chitosan matrix for boosted visible light photocatalysis for tetracycline degradation and anti-bacterial application. *J. Environ. Manag.* **2022**, *306*, 114396. [CrossRef]
78. Cheng, T.; Gao, H.; Liu, G.; Pu, Z.; Wang, S.; Yi, Z.; Wu, X.; Yang, H. Preparation of core-shell heterojunction photocatalysts by coating CdS nanoparticles onto $Bi_4Ti_3O_{12}$ hierarchical microspheres and their photocatalytic removal of organic pollutants and Cr(VI) ions. *Colloids Surf. A Physicochem. Eng. Asp.* **2022**, *633*, 127918. [CrossRef]
79. Isari, A.A.; Hayati, F.; Kakavandi, B.; Rostami, M.; Motevassel, M.; Dehghanifard, E.N. Cu co-doped TiO_2@functionalized SWCNT photocatalyst coupled with ultrasound and visible-light: An effective sono-photocatalysis process for pharmaceutical wastewaters treatment. *Chem. Eng. J.* **2020**, *392*, 123685. [CrossRef]
80. Li, R.; Cai, M.; Xie, Z.; Zhang, Q.; Zeng, Y.; Liu, H.; Liu, G.; Lv, W. Construction of heterostructured $CuFe_2O_4$/g-C_3N_4 nanocomposite as an efficient visible light photocatalyst with peroxydisulfate for the organic oxidation. *Appl. Catal. B Environ.* **2019**, *244*, 974–982. [CrossRef]
81. Shao, B.; Liu, X.; Liu, Z.; Zeng, G.; Liang, Q.; Liang, C.; Cheng, Y.; Zhang, W.; Liu, Y.; Gong, S. A novel double Z-scheme photocatalyst $Ag_3PO_4/Bi_2S_3/Bi_2O_3$ with enhanced visible-light photocatalytic performance for antibiotic degradation. *Chem. Eng. J.* **2019**, *368*, 730–745. [CrossRef]
82. Tsaryuk, V.I.; Zhuravlev, K.P.; Szostak, R.; Vologzhanina, A.V. Structure, Luminescence, and Raman Spectroscopy of Europium and Terbium Dipivaloylmethanates and Other β-Diketonates with 2,2′-Bipyridine. *J. Struct. Chem.* **2020**, *61*, 1026–1037. [CrossRef]
83. Sharma, N.D.; Singh, J.; Vijay, A.; Samanta, K.; Pandey, S.D. Investigations of anharmonic effects via phonon mode variations in nanocrystalline Dy_2O_3, Gd_2O_3 and Y_2O_3. *J. Raman Spectrosc.* **2017**, *48*, 822–828. [CrossRef]

84. Refat, M.S.; Elsabawy, K.M. Infrared spectra, Raman laser, XRD, DSC/TGA and SEM investigations on the preparations of selenium metal, (Sb_2O_3, Ga_2O_3, SnO and HgO) oxides and lead carbonate with pure grade using acetamide precursors. *Bull. Mater. Sci.* **2011**, *34*, 873–881. [CrossRef]
85. Deonikar, V.G.; Patil, S.S.; Tamboli, M.S.; Ambekar, J.D.; Kulkarni, M.V.; Panmand, R.P.; Umarji, G.G.; Shinde, M.D.; Rane, S.B.; Munirathnam, N.R.; et al. Growth study of hierarchical Ag_3PO_4/$LaCO_3OH$ heterostructures. *Phys. Chem. Chem. Phys.* **2017**, *19*, 20541–20550. [CrossRef]
86. Patil, S.S.; Tamboli, M.S.; Deonikar, V.G.; Umarji, G.G.; Ambekar, J.D.; Kulkarni, M.V.; Kolekar, S.S.; Kale, B.B.; Patil, D.R. Magnetically separable Ag_3PO_4/$NiFe_2O_4$ composites with enhanced photocatalytic activity. *Dalton T* **2015**, *44*, 20426–20434. [CrossRef]
87. Chahine, A.; Et-tabirou, M.; Pascal, J.L. FTIR and Raman spectra of the Na_2O–CuO–Bi_2O_3–P_2O_5 glasses. *Mater. Lett.* **2004**, *58*, 2776–2780. [CrossRef]
88. Li, Z.; Chen, M.; Zhang, Q.W.; Qu, J.; Ai, Z.Q.; Li, Y. J Mechanochemical synthesis of ultrafine ZnS/Zn-Al layered double hydroxide heterojunction and their photocatalytic activities in dye degradation. *Appl. Clay Sci.* **2017**, *144*, 115–120. [CrossRef]
89. Zhou, F.; Kang, K.; Maxisch, T.; Ceder, G.; Morgan, D. The electronic structure and band gap of $LiFePO_4$ and $LiMnPO_4$. *Solid. State Commun.* **2004**, *132*, 181–186. [CrossRef]
90. Tauc, J.; Grigorov, R.; Vancu, A. Optical properties and electronic structure of amorphous germanium. *Phys. Status Solidi* **1966**, *15*, 627–637. [CrossRef]
91. Butler, M.A. Photoelectrolysis with $YFeO_3$ electrodes. *J. Appl. Phys.* **1977**, *48*, 1914–1920. [CrossRef]
92. Liu, A.; Hu, J.; He, J.; Huang, X.; Hu, N.; Li, Y.; Huang, Q.; Guo, S.; Liu, X.; Yang, Z.; et al. Direct Z-scheme hierarchical heterostructures of oxygen-doped g-C_3N_4/In_2S_3 with efficient photocatalytic Cr(vi) reduction activity. *Catal. Sci. Technol.* **2021**, *11*, 7963–7972. [CrossRef]
93. Liu, B.Y.; Du, J.Y.; Ke, G.L.; Jia, B.; Huang, Y.J.; He, H.C.; Zhou, Y.; Zou, Z.G. Boosting O_2 Reduction and H_2O Dehydrogenation Kinetics: Surface N-Hydroxymethylation of g-C_3N_4 Photocatalysts for the Efficient Production of H_2O_2. *Adv. Funct. Mater.* **2022**, *32*, 2111125. [CrossRef]
94. Liu, C.; Feng, Y.; Han, Z.T.; Sun, Y.; Wang, X.Q.; Zhang, Q.F.; Zou, Z.G. Z-scheme N-doped $K_4Nb_6O_{17}$/g-C_3N_4 heterojunction with superior visible-light-driven photocatalytic activity for organic pollutant removal and hydrogen production. *Chin. J. Catal.* **2021**, *42*, 164–174. [CrossRef]
95. Chen, J.; Zhao, X.; Kim, S.G.; Park, N.G. Multifunctional Chemical Linker Imidazoleacetic Acid Hydrochloride for 21% Efficient and Stable Planar Perovskite Solar Cells. *Adv. Mater.* **2019**, *31*, 1902902. [CrossRef] [PubMed]
96. Gao, Z.W.; Wang, Y.; Ouyang, D.; Liu, H.; Huang, Z.F.; Kim, J.; Choy, W.C.H. Triple Interface Passivation Strategy-Enabled Efficient and Stable Inverted Perovskite Solar Cells. *Small Methods* **2020**, *4*, 2000478. [CrossRef]
97. Chen, J.; Kim, S.-G.; Ren, X.; Jung, H.S.; Park, N.-G. Effect of bidentate and tridentate additives on the photovoltaic performance and stability of perovskite solar cells. *J. Mater. Chem. A* **2019**, *7*, 4977–4987. [CrossRef]
98. Ma, Q.; Kumar, R.K.; Xu, S.Y.; Koppens, F.H.L.; Song, J.C.W. Photocurrent as a multiphysics diagnostic of quantum materials. *Nat. Rev. Phys.* **2023**, *5*, 170–184. [CrossRef]
99. Cheng, Y.X.; Ye, J.H.; Lai, L.; Fang, S.; Guo, D.Y. Ambipolarity Regulation of Deep-UV Photocurrent by Controlling Crystalline Phases in Ga_2O_3 Nanostructure for Switchable Logic Applications. *Adv. Electron. Mater.* **2023**, *9*, 2201216. [CrossRef]
100. Cheng, T.; Gao, H.; Sun, X.; Xian, T.; Wang, S.; Yi, Z.; Liu, G.; Wang, X.; Yang, H. An excellent Z-scheme Ag_2MoO_4/$Bi4Ti_3O_{12}$ heterojunction photocatalyst: Construction strategy and application in environmental purification. *Adv. Powder Technol.* **2021**, *32*, 951–962. [CrossRef]
101. Jiang, L.B.; Yuan, X.Z.; Zeng, G.M.; Liang, J.; Chen, X.H.; Yu, H.B.; Wang, H.; Wu, Z.B.; Zhang, J.; Xiong, T. In-situ synthesis of direct solid-state dual Z-scheme WO_3/g-C_3N_4/Bi_2O_3 photocatalyst for the degradation of refractory pollutant. *Appl. Catal. B* **2018**, *227*, 376–385. [CrossRef]